CrossMark

# Chemical and isotopic features of cold and thermal fluids discharged in the Southern Volcanic Zone between 32.5°S and 36°S: Insights into the physical and chemical processes controlling fluid geochemistry in geothermal systems of Central Chile

O. Benavente [a,b,*], F. Tassi [c,d], M. Reich [a,b], F. Aguilera [e], F. Capecchiacci [d,e], F. Gutiérrez [a,b], O. Vaselli [c,d], A. Rizzo [f]

[a] Departamento de Geología, Universidad de Chile, Plaza Ercilla 803, Santiago, Chile
[b] Centro de Excelencia en Geotermia de los Andes (CEGA), Universidad de Chile, Plaza Ercilla 803, 8370450, Santiago, Chile
[c] Dipartimento di Scienze della Terra, Via G. La Pira 4, 50121 Firenze, Italy
[d] CNR-IGG Istituto di Geoscienze e Georisorse, Via G. La Pira 4, 50121 Firenze, Italy
[e] Servicio Nacional de Geología y Minería, Av. Santa María Chaina 0104, Santiago, Chile
[f] Istituto Nazionale Geofisica e Vulcanologia INGV, Sez. di Palermo, Via U. La Malfa 153, 90145 Palermo, Italy

## ARTICLE INFO

## ABSTRACT

The Principal Cordillera of Central Chile is characterized by two belts of different ages and lithologies: (i) an eastern Mesozoic belt, consisting of limestone- and gypsum-rich sedimentary rocks at the border between Central Chile and Argentina, where the active volcanic arc occurs; and (ii) a western belt of Cenozoic age containing basaltic to andesitic volcanic and volcanoclastic sequences. This distinctive geological setting controls water chemistry of cold and thermal springs in the region, which are fed by meteoric water that circulates through deep regional structures. In the western sector of Principal Cordillera, water–rock interaction processes produce low TDS, slightly alkaline $HCO_3^-$ dominated waters, although dissolution of underlying Mesozoic evaporitic rocks occasionally causes $SO_4^{2-}$ and $Cl^-$ enrichments. In this area, few $Na^+$–$HCO_3^-$ and $Na^+$–$SO_4^{2-}$ waters occurred, being likely produced by a $Ca^{2+}$–$Na^+$ exchange during water–rock interactions. Differently, the chemical features of $Ca^{2+}$–$Cl^-$ waters was likely related to an albitization–chloritization process affecting basaltic to andesitic rocks outcropping in this area. Addition of $Na^+$–$Cl^-$ brines uprising from the eastern sector through the west-verging thrust faults cannot be excluded, as suggested by the occurrence of mantle He (~19%) in dissolved gases. In contrast, in the eastern sector of the study region, mainly characterized by the occurrence of evaporitic sequences and relatively high heat flow, mature $Na^+$–$Cl^-$ waters were recognized, the latter being likely related to promising geothermal reservoirs, as supported by the chemical composition of the associated bubbling and fumarolic gases. Their relatively low $^3He/^4He$ ratios (up to 3.9 Ra) measured in the fumaroles on this area evidenced a significant crustal contamination by radiogenic $^4He$. The latter was likely due to (i) degassing from $^4He$-rich magma batches residing in the crust, and/or (ii) addition of fluids interacting with sedimentary rocks. This interpretation is consistent with the measured $\delta^{13}C$-$CO_2$ values (from −13.2 to −5.72‰ vs. V-PDB) and the $CO_2/^3He$ ratios (up to $14.6 \times 10^{10}$), which suggest that $CO_2$ mostly originates from the limestone-rich basement and recycling of subducted sediments, with an important addition of sedimentary (organic-derived) carbon, whereas mantle degassing contributes at a minor extent. According to geothermometric estimations based on the $Na^+$, $K^+$, $Mg^{2+}$ and $Ca^{2+}$ contents, the mature $Na^+$–$Cl^-$ rich waters approached a chemical equilibrium with calcite, dolomite, anhydrite, fluorite, albite, K-feldspar and Ca- and Mg-saponites at a broad range of temperatures (up to ~300 °C) In the associated gas phase, equilibria of chemical reactions characterized by slow kinetics (e.g. sabatier reaction) suggested significant contributions from hot and oxidizing magmatic gases. This hypothesis is consistent with the $\delta^{13}C$-$CO_2$, Rc/Ra, $CO_2/^3He$ values of the fumarolic gases. Accordingly, the isotopic signatures of the fumarolic steam is similar to that of fluids discharged from the summit craters of the two active volcanoes in the study area (Tupungatito and Planchón–Peteroa). These results encourage the development of further geochemical and geophysical surveys aimed to provide an exhaustive evaluation of the geothermal potential of these volcanic–hydrothermal systems.

© 2015 Elsevier B.V. All rights reserved.

* Corresponding author at: Departamento de Geología, Universidad de Chile, Plaza Ercilla 803, Santiago, Chile.
E-mail address: obenaven@ing.uchile.cl (O. Benavente).

## 1. Introduction

The Andes of Central Chile (32.5–36°S) is an active subduction-related mountain belt that hosts a number of hydrothermal systems feeding dozens thermal fluid discharges (Fig. 1; Hauser, 1997). In this region, the interplay between magmatism and hydrothermal fluid circulation has produced some of the world's largest mineral deposits, including Cu-porphyry, Au–Cu veins, Cu-skarn, and epithermal Au deposits (Maksaev et al., 2007; Stern et al., 2007). Nowadays, heat flow anomalies, active volcanoes and geothermal systems (Fig. 2a, b) seem related to the regional tectono-magmatic setting dominated by N–S- and NE–SW-trending thrust faults (Hamza and Muñoz, 1996; Hauser, 1997). According to preliminary surveys carried out by ENAP (Chilean National Oil Company), four promising areas, with an estimated geothermal potential ranging between 400 and 1300 MW$_e$ (Soffia, 2004), were recognized in this sector of the Andes: (i) San José, (ii) Tinguiririca, (iii) Calabozos, and (iv) Mariposas. At Mariposas, measured temperatures in boreholes drilled at 659, 897 and 1074 m depth ranged from 190 to 204 °C (Hickson et al., 2011), whereas at Tinguiririca temperatures up to 235 °C were measured at ~800 m depth (Clavero et al., 2011; Droguett et al., 2012). Despite their significant potential, the geothermal exploitation is still a challenge in Chile, mainly due to social, political and economic reasons (Hall et al., 2009; Dufey, 2010; Barnett, 2012; Hodgson, 2013; Sanchez-Alfaro et al., 2015).

A preliminary survey of the chemical characteristics of the thermal springs in the study area was carried out by Hauser (1997), who proposed the occurrence of two main fluid domains. The first domain refers to the north-western sector of Principal Cordillera (PC) from 32.5°S to 34°S (Fig. 2a), where a heat flow up to ~60 mW/m$^2$ was estimated (Hamza and Muñoz, 1996). Cold and thermal waters, mostly located along the San Ramón–Pocuro fault system (Fig. 2b), showed relatively low values of total dissolved solids (TDS <2000 mg/L). The second domain, corresponding to the south-eastern sector of PC from 35°S to 36°S (Fig. 2a), is marked by an anomalously high heat flow (up to 220 mW/m$^2$; Hamza and Muñoz, 1996), and hosts thermal springs with relatively high TDS values (up to 20,000 mg/L). A geochemical study focused on the He isotope ratios from geothermal fluids and rocks from a wide region of the Andes (Hilton et al., 1993) reported two relatively low Rc/Ra values for gases from this domain (2.16 and 1.56 for Baños Morales and Termas Cauquenes, respectively). To the best of our knowledge, more detailed information on the geochemical features of these fluid discharges is currently not available. The present study is thus aimed to fill this gap by presenting and discussing original chemical and isotopic ($^3$He/$^4$He, $\delta^{18}$O-H$_2$O, $\delta$D-H$_2$O, $\delta^{13}$C-CO$_2$) data of water and gas samples collected from 49 cold and thermal springs, including bubbling pools and fumarolic vents, from different areas of this sector of PC. The main aims are to i) constrain the main source region(s) and the physico-chemical processes controlling the chemistry of the discharged fluids, ii) discuss the role played by the regional geotectonic setting, and iii) produce a geochemical dataset of hydrothermal–magmatic fluids in order to provide indication useful for the future exploitation of the geothermal resources of Central Chile.

## 2. Tectonic, geological and volcanological setting

The geodynamic setting of the Andes in Central Chile is controlled by the subduction of the oceanic Nazca plate below the continental lithosphere of the western side of South America (Fig. 1; Farías et al., 2010). The sector of the Andes range in the study area includes the northern region (33–36°S) of the Southern Volcanic Zone (SVZ; 33–46°S), showing a slab dip >25°. This area is bounded to the north (32.5°S) by the Pampean flat-slab segment (28–32.5°S), where the slab dip is <10° at depths from 100 to 150 km (Barazangi and Isacks, 1976; Tassara et al., 2006; Stern et al., 2007). This flat-slab segment, where volcanic activity has not occurred in the last 9 My, was interpreted as the result of buoyancy force exerted by the subduction

of the Juan Fernández ridge (Pilger, 1981; Yáñez et al., 2001; Tassara et al., 2006). According to Farías et al. (2010), other distinctive geotectonic features related to the subduction of the Juan Fernández ridge are, as follows: i) the northward increase of the maximum elevations along the Andean chain from ~3500 to <7000 m a.s.l., ii) an increase from south to north of the crustal thickness from <40 km to ~60 km, and iii) a decrease, in the same direction, of the asthenospheric mantle wedge thickness from ~70 to 20 km (Tassara et al., 2006).

The Maipo orocline, i.e. the arcuate shape of the Andean orogen at 34.5°S (Fig. 2a), marks a volcano-tectonic limit between the northern (32.5–34.5°S) and the southern (34.5–36°S) zones (Cembrano and Lara, 2009; Farías et al., 2010; Arriagada et al., 2013). The former is characterized by a compressional regime and N–S-oriented tectonic structures, whereas the latter shows a dextral transpressional regime and NNE–SSW-oriented tectonic structures (Cembrano and Lara, 2009). In both zones, three-parallel morphostructural units can be recognized from west to east (Farías et al., 2010), as follows: (i) Coastal Cordillera, (ii) Central Depression, and (iii) Principal Cordillera (PC) (Fig. 2a). Cenozoic deposits (basaltic to andesitic volcanic–volcanoclastic rocks) occur between the eastern side of the Central Depression and the western PC (WPC), where the structural assessment is controlled by the
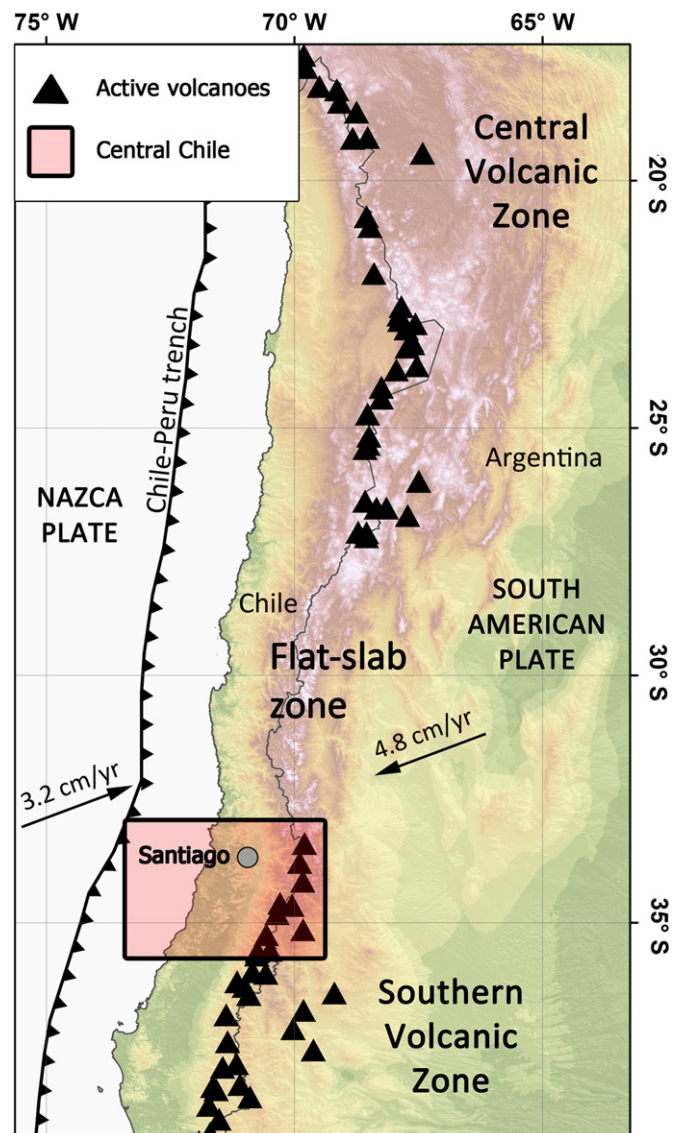


**Fig. 1.** Map of Central Chile with the location of the Holocene volcanoes along the Central and Southern Volcanic Zones.
The reported absolute plate motion velocity is from Gripp and Gordon (2002).
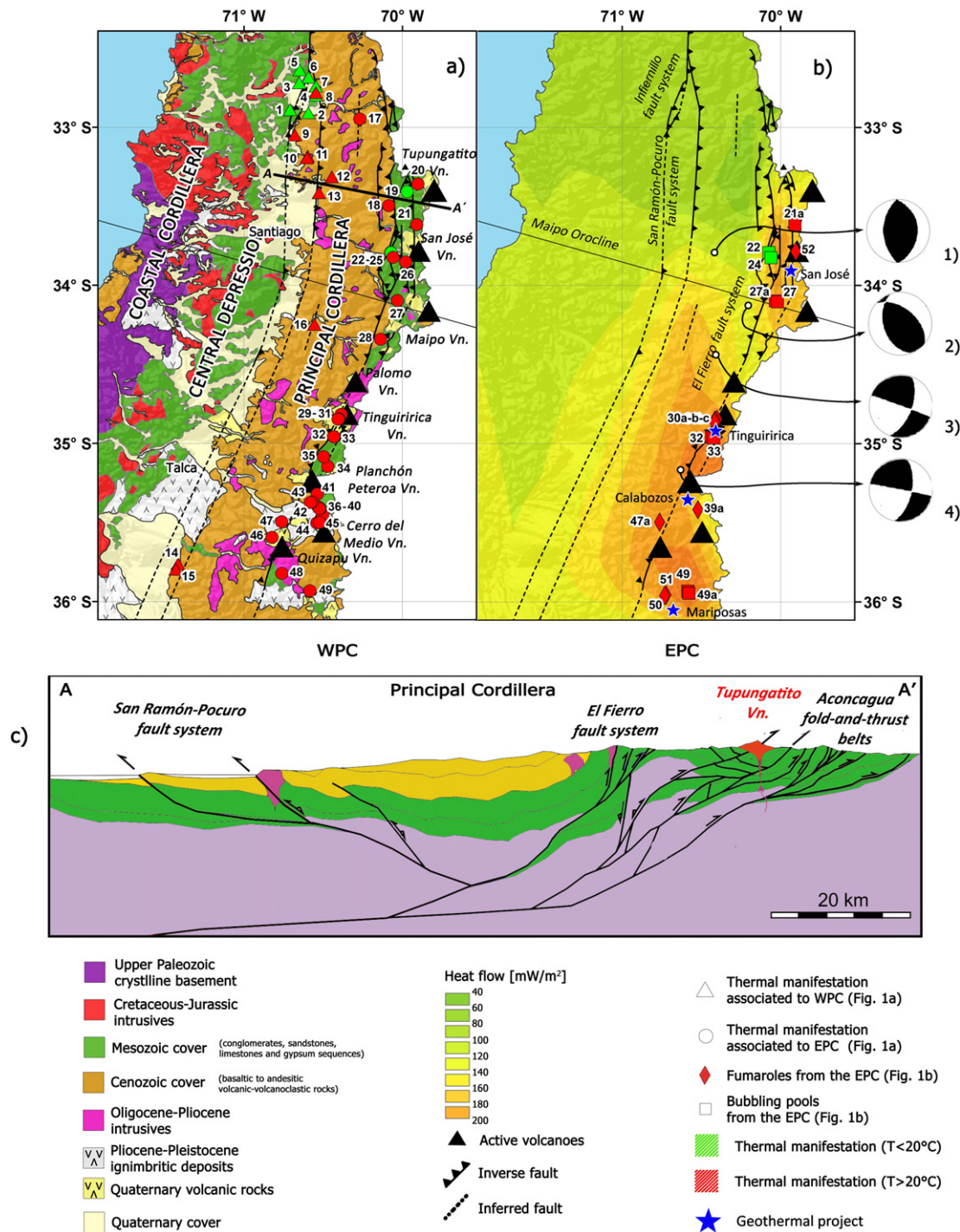
**Fig. 2.** (a) Geological and morphological map of Central Chile (Farías et al., 2007, 2010). Symbols are, as follows: red triangle: thermal springs from the Western Principal Cordillera (WPC); green triangle: cold springs from the WPC; red circle: thermal springs from the Eastern Principal Cordillera (EPC); green circle: cold springs from the EPC; black triangle: active volcanoes. (b) Tectonic assessment and heat flow pattern (Giambiagi et al., 2014). Symbols are, as follows: red diamond: fumaroles; green square: cold bubbling pool; red square: hot bubbling pools. (c) Regional geological–structural cross section of Central Chile through the Tupungatito volcano (modified from Giambiagi et al., 2014).

W-vergent Infiernillo and San Ramón–Pocuro thrust faults (Fig. 2b). Along the eastern zone of PC (EPC), W-vergent folds and faults subtly deform the 5500 m thick basaltic to andesitic volcanic–volcanoclastic Cenozoic sequences (Fig. 2c; Charrier et al., 2002). East of the high-angle reverse El Fierro fault system (EPC), where E-verging fold-and-thrust belts occur (Fig. 2c; Giambiagi et al., 2003), Mesozoic conglomerates, sandstones, limestones and gypsum sequences outcrop (Fig. 2c).

In the northern area, active volcanoes occur on the top of the Mesozoic basement, whereas south of 34.5°S they are located at the Meso-Cenozoic boundary (Fig. 2a). Volcanic products from the Quaternary volcanic chain are tholeiitic basalts to high-K rhyolites (Stern et al., 2007). Andesites are the most abundant products, although basalts increase southward (Hildreth and Moorbath, 1988). Volcanic rocks north of the Maipo orocline are characterized by (i) higher contents of incompatible trace elements with respect to those measured in the rocks from south of 34.5°S, (ii) $^{87}Sr/^{86}Sr$ and $^{143}Nd/^{144}Nd$ ratios up to 0.70566 and 0.5129, respectively, and (iii) K/Rb < 200 (Hildreth and Moorbath, 1988). These petrochemical features indicate an N–S

**Table 1**

Chemical and stable isotopic ($\delta^{18}$O-H$_2$O and $\delta$D-H$_2$O, in ‰ vs. V-SMOW) composition of cold (T < 20 °C) and thermal (T > 20 °C) waters from Central Chile. Concentrations are in mg/L. Geographic coordinates (UTM; WGS-84 19S), altitude (m), outlet temperature (°C) and pH values are also reported.

| ID | Name | type | Date | zone | Coord N | Coord E | Altitude | T | pH | TDS | $Ca^{2+}$ | $K^+$ | $Mg^{2+}$ | $Na^+$ | $Li^+$ | $F^-$ | $Cl^-$ | $Br^-$ | $NO_3^-$ | $SO_4^{2-}$ | $HCO_3^-$ | $CO_3^{2-}$ | B | $\delta$D-H$_2$O | $\delta^{18}$O-H$_2$O |
|---|---|---|---|---|---|---|---|---|---|---|---|---|---|---|---|---|---|---|---|---|---|---|---|---|---|
| 1 | Auco | Spring | 1/15/2011 | WPC | 6359740 | 340130 | 846 | 18.7 | 7.7 | 416 | 65 | 0.2 | 10 | 30 | 0.01 | 0.14 | 5.5 | 0.04 | 15 | 80 | 180 | | 0.17 | −72.0 | −9.6 |
| 2 | El Barro | Spring | 1/15/2011 | WPC | 6376500 | 355078 | 1060 | 15.4 | 7.3 | 551 | 80 | 0.2 | 20 | 30 | 0.03 | 0.10 | 3.3 | 0.04 | 20 | 75 | 290 | | 0.09 | −82.1 | −10.7 |
| 3 | El Corazon | Spring | 1/14/2011 | WPC | 6369980 | 355075 | 940 | 19.0 | 7.8 | 365 | 50 | 0.2 | 12 | 30 | 0.03 | 0.11 | 8.3 | 0.05 | 8.0 | 38 | 189 | | 0.05 | −76.0 | −9.7 |
| 4 | El Lobo | Spring | 1/16/2011 | WPC | 6371960 | 355194 | 938 | 20.1 | 7.0 | 696 | 115 | 0.5 | 35 | 30 | 0.03 | 0.34 | 3.0 | 0.04 | 4.0 | 300 | 170 | | 0.06 | −72.9 | −9.3 |
| 5 | El Parrón | Spring | 1/14/2011 | WPC | 6387650 | 345420 | 1910 | 12.8 | 7.5 | 295 | 42 | 0.5 | 4.0 | 22 | 0.01 | 0.05 | 2.5 | 0.03 | 9.6 | 11 | 170 | | 0.07 | −80.0 | −10.9 |
| 6 | Jahuel | Spring | 1/14/2011 | WPC | 6382649 | 350698 | 1127 | 16.8 | 7.4 | 537 | 75 | 1.9 | 23 | 34 | 0.02 | 0.35 | 5.0 | 0.05 | 5.1 | 200 | 160 | | 0.10 | −83.9 | −11.0 |
| 7 | La Higuera | Spring | 1/16/2011 | WPC | 6378760 | 345286 | 794 | 11.0 | 7.6 | 466 | 73 | 0.5 | 13 | 15 | 0.03 | 0.10 | 4.5 | 0.04 | 3.9 | 46 | 260 | | 0.07 | −71.5 | −9.5 |
| 8 | La Totora | Spring | 1/16/2011 | WPC | 6357715 | 350908 | 1010 | 12.0 | 7.5 | 419 | 66 | 0.4 | 8.0 | 24 | 0.02 | 0.20 | 13 | 0.02 | 5.6 | 92 | 180 | | 0.07 | −91.9 | −12.8 |
| 9 | Baños de Chacabuco | Spring | 1/17/2011 | WPC | 6341956 | 343311 | 741 | 23.5 | 7.6 | 338 | 24 | 0.8 | 0.9 | 80 | 0.13 | 0.11 | 29 | 1.3 | 7.8 | 87 | 90 | | 0.60 | | |
| 10 | Termas de Colina | Spring | 1/17/2011 | WPC | 6327245 | 351014 | 948 | 29.0 | 7.8 | 449 | 50 | 0.9 | 1.2 | 83 | 0.04 | 0.12 | 100 | 0.27 | 7.9 | 120 | 60 | | 1.3 | −67.2 | −9.0 |
| 11 | Baños el Carvajalino | Spring | 1/17/2011 | WPC | 6326085 | 350565 | 819 | 24.9 | 7.9 | 420 | 53 | 0.7 | 2.2 | 68 | 0.10 | 0.02 | 87 | 1.40 | 4.9 | 115 | 68 | | 0.16 | | |
| 12 | Termas de la Cal | Spring | 1/18/2011 | WPC | 6312927 | 365418 | 1167 | 20.0 | 8.1 | 209 | 28 | 0.3 | 3.5 | 24 | 0.18 | 0.01 | 14 | 0.05 | 8.4 | 21 | 87 | | 2.1 | −68.2 | −9.3 |
| 13 | Baños de Apoquindo | Spring | 1/18/2011 | WPC | 6301705 | 358122 | 857 | 21.1 | 7.7 | 1704 | 375 | 1.3 | 2.6 | 232 | 0.03 | 0.01 | 870 | 4.1 | 4.8 | 100 | 93 | | 0.07 | | |
| 14 | Termas Panimávida | Spring | 3/20/2010 | WPC | 6,09,846 | 281,522 | 970 | 33.7 | 9.3 | 339 | 30 | 1.3 | 0.33 | 57 | 0.09 | 0.34 | 53 | 2.2 | 1.5 | 152 | 5.5 | 3.6 | 1.57 | −58.6 | −9.0 |
| 15 | Termas Quinamávida | Spring | 3/20/2010 | WPC | 603588 | 280284 | 970 | 23.3 | 9.2 | 296 | 18 | 1.5 | 0.2 | 54 | 0.15 | 0.22 | 3.5 | 0.03 | 1.6 | 8.7 | 156 | 13 | 0.42 | −50.9 | −7.8 |
| 16 | Cauquenes | Spring | 1/10/2013 | WPC | 6209276 | 356744 | 756 | 45.7 | 6.3 | 3382 | 778 | 9.3 | 0.3 | 464 | 1.2 | 0.01 | 1977 | 8.6 | 7.7 | 62 | 30 | | 6.3 | −58.8 | −8.6 |
| 17 | Saladillo | Spring | 1/9/2013 | EPC | 6353643 | 381298 | 1716 | 21.9 | 7.6 | 13,485 | 728 | 121 | 44 | 3793 | 6.1 | 0.03 | 7844 | 14 | 8.2 | 713 | 162 | | 7.2 | −100 | −13.8 |
| 18 | Salinilla | Spring | 2/21/2011 | EPC | 6293034 | 399001 | 1680 | 22.7 | 7.1 | 11,710 | 461 | 39 | 46 | 3985 | 5.8 | 0.26 | 6386 | 12 | 1.1 | 480 | 244 | | 1.3 | | |
| 19 | Baños Azules | Spring | 2/21/2011 | EPC | 6302976 | 409612 | 2504 | 17.8 | 5.1 | 2749 | 612 | 6.4 | 62 | 62 | 0.50 | 2.2 | 69 | 0.09 | 0.50 | 1063 | 828 | | 0.14 | −95.2 | −13.1 |
| 20 | Termas Tupungato | Spring | 2/21/2011 | EPC | 6308503 | 415987 | 2975 | 24.2 | 5.1 | 4094 | 684 | 37 | 126 | 319 | 1.1 | 2.0 | 381 | 0.50 | 2.5 | 1762 | 710 | | 4.1 | | |
| 21 | Termas del Plomo 1 | Bubbling pool | 2/10/2013 | EPC | 6279865 | 415546 | 2978 | 26.8 | 7.1 | 8892 | 518 | 14 | 91 | 2707 | 3.97 | 0.01 | 3763 | 7.4 | 4.9 | 1610 | 142 | | 0.83 | −104 | −15.6 |
| 22 | Monumento Morado 1 | Bubbling pool | 2/13/2013 | EPC | 6260255 | 400543 | 2265 | 9.1 | 7.3 | 3335 | 633 | 7.7 | 94 | 39 | 0.68 | 0.02 | 20 | 0.01 | 1.8 | 440 | 2056 | | 0.21 | −95.0 | −13.0 |
| 23 | Monumento Morado 2 | Bubbling pool | 2/13/2013 | EPC | 6260176 | 400649 | 2264 | 10.4 | 7.5 | 4990 | 1094 | 6.6 | 92 | 42 | 0.44 | 0.02 | 21 | 0.02 | 1.5 | 807 | 2863 | | 2.3 | −101 | −13.5 |
| 24 | Baños Morales P1 | Bubbling pool | 1/11/2013 | EPC | 6256821 | 401927 | 1812 | 15.2 | 6.2 | 7457 | 461 | 83 | 72 | 2024 | 3.67 | 0.30 | 3785 | 7.6 | 5.1 | 427 | 540 | | 1.8 | −105 | −13.6 |
| 25 | Baños Morales P2 | Spring | 1/20/2011 | EPC | 6256821 | 401927 | 1812 | 28.2 | 6.2 | 28,503 | 1093 | 279 | 231 | 9125 | 15 | 0.41 | 15,184 | 45 | 5.7 | 1016 | 1420 | | 3.3 | | |
| 26 | Baños Colina | Spring | 1/17/2011 | EPC | 6253744 | 409262 | 2545 | 51.3 | 6.4 | 31,513 | 1416 | 342 | 314 | 9950 | 14 | 0.56 | 15,283 | 51 | 3.3 | 2964 | 992 | | 19 | −96.3 | −13.4 |

| No. | Name | Type | Date | | | | | | | | | | | | | | | | | | | | | | |
|---|---|---|---|---|---|---|---|---|---|---|---|---|---|---|---|---|---|---|---|---|---|---|---|---|---|
| 27 | Puente de Tierra 1 | Bubbling pool | 2/1/2013 | EPC | 6226554 | 404731 | 2148 | 45.0 | 6.5 | 56,743 | 1626 | 343 | 263 | 18,324 | 44 | 0.02 | 31,806 | 58 | 47 | 2848 | 1305 | | 19.4 | −107 | −13.6 |
| 28 | Baños Las Calerías | Spring | 1/11/2013 | EPC | 6199348 | 395156 | 2190 | 61.0 | 6.3 | 9514 | 730 | 203 | 39 | 2360 | 10 | 0.20 | 3590 | 9.2 | 0.30 | 1620 | 830 | | 42 | −106 | −13.3 |
| 29 | Termas Azufre | Spring | 1/27/2013 | EPC | 6146230 | 373120 | 3157 | 27.5 | 2.9 | 922 | 74 | 2.1 | 24 | 54 | 0.16 | 2.8 | 98 | 0.11 | 0.13 | 567 | | | 0.03 | −93.0 | −12.9 |
| 30 | Baños Los Humos 1 | Bubbling pool | 1/25/2013 | EPC | 6143023 | 371798 | 2974 | 24.0 | 1.8 | 435 | 60 | 1.1 | 11 | 21 | 0.16 | 0.29 | 9.3 | 0.03 | 0.19 | 311 | | | 0.03 | −63.0 | −5.7 |
| 31 | Campamento Humos | Spring | 1/25/2013 | EPC | 6142895 | 371250 | 2726 | 59.7 | 6.8 | 584 | 61 | 1.5 | 10 | 50 | 0.21 | 0.22 | 9.2 | 0.02 | 0.13 | 37 | 394 | | 1.6 | −90.0 | −12.8 |
| 32 | Termas del Flaco 1 | Bubbling pool | 3/25/2012 | EPC | 6130555 | 368978 | 1806 | 63.7 | 6.9 | 3888 | 139 | 128 | 5.9 | 1182 | 3.9 | 1.8 | 1801 | 3.2 | 1.8 | 288 | 170 | | 14 | −95.1 | −12.2 |
| 33 | Termas del Flaco 2 | Bubbling pool | 3/25/2012 | EPC | 6130555 | 368996 | 1732 | 89.4 | 6.9 | 3624 | 135 | 119 | 5.2 | 1135 | 4.3 | 7.7 | 1652 | 2.7 | 1.5 | 287 | 183 | | 16 | −91.1 | −11.5 |
| 34 | Termas de San Pedro | Spring | 3/19/2011 | EPC | 6109783 | 365777 | 1732 | 24.0 | 7.1 | 15,542 | 768 | 729 | 25 | 3698 | 3.1 | 7.1 | 8390 | 128 | 11 | 1177 | 564 | | 9.9 | −96.8 | −13.3 |
| 35 | Termas Romeral | Spring | 3/19/2011 | EPC | 6116454 | 363400 | 1433 | 60.0 | 8.6 | 1784 | 141 | 25 | 7.3 | 464 | 0.75 | 0.12 | 911 | 1.7 | 2.8 | 119 | 96 | 1.1 | 1.7 | −92.3 | −13.7 |
| 36 | Termas del Tigre Naciente | Spring | 3/14/2011 | EPC | 6073577 | 362754 | 2563 | 64.9 | 7.2 | 718 | 21 | 3.1 | 1.1 | 146 | 0.44 | 4.6 | 95 | 0.15 | 1.5 | 110 | 275 | | 4.6 | −95.1 | −13.3 |
| 37 | Termas Potrerillo | Spring | 3/14/2011 | EPC | 6075560 | 363420 | 2343 | 46.0 | 7.4 | 930 | 65 | 5.4 | 5.4 | 180 | 0.27 | 3.0 | 53 | 0.13 | 1.5 | 265 | 295 | | 0.66 | −96.1 | −13.5 |
| 38 | Termas del Pellejo | Spring | 3/14/2011 | EPC | 6081288 | 360694 | 2129 | 48.9 | 6.7 | 1648 | 125 | 21 | 32 | 194 | 0.45 | 2.6 | 195 | 0.56 | 1.5 | 135 | 813 | | 2.5 | −96.3 | −13.4 |
| 39 | Barro Colorado 1 | Spring | 3/14/2011 | EPC | 6080029 | 361881 | 2154 | 75.0 | 7.4 | 2767 | 80 | 67 | 6.3 | 860 | 1.9 | 1.7 | 1244 | 12 | 1.5 | 106 | 245 | | 5.5 | −94.4 | −12.8 |
| 40 | Termas de la Quebrada de los Colores | Spring | 3/15/2010 | EPC | 6080040 | 361386 | 2185 | 30.2 | 6.8 | 2550 | 292 | 8.5 | 94 | 220 | 0.68 | 1.4 | 40 | 0.09 | 1.5 | 375 | 1434 | | 1.0 | −95.5 | −13.6 |
| 41 | Fumaroles del Azufre | Spring | 3/15/2010 | EPC | 6090191 | 360011 | 2738 | 70.0 | 5.4 | 823 | 63 | 11 | 24 | 60 | 0.15 | 0.25 | 3.7 | 0.02 | 1.6 | 2.5 | 485 | | | −91.2 | −11.1 |
| 42 | Termas Baños de la Yegua | Spring | 3/15/2010 | EPC | 6084620 | 357295 | 1995 | 54.0 | 6.7 | 3039 | 314 | 53 | 15 | 605 | 1.2 | 2.1 | 724 | 0.85 | 1.5 | 498 | 680 | | 7.8 | −94.8 | −13.0 |
| 43 | Fumarolas de Llolli | Spring | 3/15/2010 | EPC | 6084260 | 356196 | 2002 | 94.5 | 2.0 | 2071 | 49 | 15 | 28 | 37 | 0.16 | 0.17 | 1.7 | 0.15 | 1.3 | 1657 | | | 0.03 | −60.7 | −4.2 |
| 44 | Termas de Aguas Calientes 1 | Spring | 3/14/2010 | EPC | 6069989 | 360200 | 2569 | 38.9 | 6.9 | 622 | 44 | 4.0 | 5.9 | 114 | 0.36 | 2.1 | 61 | 0.12 | 1.9 | 80 | 262 | | 0.89 | | |
| 45 | Termas de Aguas Calientes 2 | Spring | 3/14/2010 | EPC | 6070203 | 361680 | 2563 | 37.9 | 7.0 | 671 | 45 | 3.7 | 5.5 | 98 | 0.31 | 1.7 | 71 | 0.15 | 1.6 | 84 | 315 | | 1.2 | −86.6 | −13.3 |
| 46 | Termas del Descabezado Grande | Spring | 1/14/2012 | EPC | 6059316 | 334606 | 1880 | 29.8 | 5.8 | 1248 | 54 | 24 | 101 | 111 | 0.25 | 0.35 | 101 | 0.16 | 1.5 | 137 | 612 | | 5.4 | −87.3 | −13.3 |
| 47 | Estero del Volcán 1 | Spring | 1/15/2012 | EPC | 6070460 | 340000 | 1954 | 79.5 | 6.0 | 926 | 81 | 3.9 | 23 | 94 | 0.17 | 3.1 | 2.4 | 0.02 | 1.5 | 65 | 497 | | 0.60 | −83.5 | −11.7 |
| 48 | Termas del Medano | Spring | 2/15/2013 | EPC | 6034171 | 340794 | 988 | 29.5 | 6.6 | 939 | 104 | 7.9 | 5.1 | 134 | 0.56 | 0.67 | 331 | 0.79 | 1.5 | 266 | 37 | | 10 | −89.5 | −12.4 |
| 49 | Termas del Campanario 1 | Bubbling pool | 2/15/2013 | EPC | 6022199 | 356881 | 1545 | 45.7 | 6.3 | 20,897 | 1925 | 340 | 85 | 5335 | 17 | 0.03 | 12,061 | 37 | 1.2 | 508 | 517 | | 3.0 | −101 | −13.6 |

increasing trend of continental crust assimilation by magmas (Hildreth and Moorbath, 1988; Cembrano and Lara, 2009). This would imply that the magma batches north of the Maipo orocline have relatively long residence times in the crust. According to Cembrano and Lara (2009), this is related to the fact that the thrust faults that serve as magma conduits are severely misoriented (dipping >45°) with respect to the prevailing compressive stress field (Sibson, 1996, 2007; Cox, 2010). On the other hand, south of the Maipo orocline (Fig. 2b) the occurrence of a thinner crust and NNE-striking thrust faults favorably oriented for strike-slip deformation (Sibson, 1996, 2007; Cox, 2010) favors the magma ascent through NE-striking fractures, which explains the relatively low residence time of magmas in the crust (Cembrano and Lara, 2009).

## 3. Sampling and analytical methods

### 3.1. Waters

Temperature and pH were measured in situ with portable instruments (uncertainties: ±0.1 °C and ±0.05, respectively). Main anions ($HCO_3^-$, $Cl^-$, $SO_4^{2-}$, $F^-$, $Br^-$ and $NO_3^-$) and B were analyzed in filtered (0.45 μm) samples, whereas cations ($Na^+$, $K^+$, $Ca^{2+}$, $Mg^{2+}$ and $Li^+$) were analyzed in filtered-acidified (with ultrapure HCl) samples. Total alkalinity (expressed as $HCO_3^-$) was determined by acid titration (AT) using HCl 0.01 N and methyl-orange as the indicator. The $CO_3^{2-}$ concentrations in waters with pH > 8.3 were calculated stoichiometrically. Anions and cations were analyzed by ion-chromatography (IC) using a Metrohm 861 and a Metrohm 761, respectively. Boron was analyzed using the Azomethine-H method (AH, Bencini, 1985) by molecular spectrophotometry (Philips UNICAM). The analytical errors for AT, IC and AH analyses were ≤5%.

The $^{18}O/^{16}O$ and $^2H/^1H$ ratios in water (expressed as $\delta^{18}O$-$H_2O$ and $\delta D$-$H_2O$ ‰ vs. V-SMOW, respectively) were analyzed in samples collected in 50 mL sterile opaque glass bottles by using a Finnigan MAT 252 and an Europa Scientific GEO2020 mass spectrometers, respectively. Oxygen isotopic ratios were analyzed in $CO_2$ added to the water samples using the $CO_2$–$H_2O$ equilibration method proposed by Epstein and Mayeda (1953). Hydrogen isotopic ratios were measured on $H_2$ after the reaction of water (10 μL) with metallic magnesium (1.6 g) at 440 °C. The analytical uncertainties for $\delta^{18}O$-$H_2O$ and $\delta D$-$H_2O$ ratios were 0.1‰ and 1‰, respectively.

### 3.2. Gases

Gas samples from fumarolic vents and bubbling pools were collected using pre-evacuated, 60 mL Giggenbach-type flasks (Giggenbach, 1975) filled with 20 mL of 4 N NaOH and a 0.15 M Cd(OH)$_2$ suspension (Montegrossi et al., 2001; Vaselli et al., 2006). Gas samples from fumarolic vents were conveyed into the sampling flasks using a 1-m-long titanium tube ($\varnothing$ = 2.5 cm) that was inserted into the fumarolic vent and connected through glass dewar tubes. Gas samples from bubbling pools were collected using a plastic funnel connected to the sampling flasks through tygon tubes. At each sampling site, a 60 mL glass pre-evacuated vial was used to collect a sample for the analysis of carbon isotopes in $CO_2$ using the same sampling apparatus adopted for the soda flasks. Gases dissolved in waters were sampled using pre-evacuated 250 mL glass vials equipped with a Teflon stopcock. Sampling flasks were filled with water up to ¾ of the flasks inner volume (Caliro et al., 2008). Gases ($CO_2$, $N_2$, Ar, $O_2$, $CH_4$, $H_2$, and He) in the headspace of both the Giggenbach-type flasks and those used for the collection of dissolved gases were analyzed at the Department of Earth Sciences of the University of Florence (Italy) by gas-chromatography (GC) using a Shimadzu 15A equipped with a 10 m long 5A-molecular sieve column and a thermal conductivity detector (TCD) (Vaselli et al., 2006). Argon and $O_2$ were analyzed using a Thermo Focus gas chromatograph equipped with a 30 m long capillary molecular sieve column and a TCD. The liquid and the solid precipitate in the alkaline suspension

were separated by centrifugation at 4000 rpm for 30 min. The liquid phase was used to analyze $CO_2$, as $CO_3^{2-}$ by AT (Metrohm Basic Titrino) with a 0.5 N HCl solution. CdS in the solid precipitate was oxidized to $SO_4^{2-}$ using $H_2O_2$ and analyzed by IC (Methrom 761) for determining the $H_2S$ concentrations. The analytical errors for AT, GC and IC analyses were ≤7%.

The analysis of $^{13}C/^{12}C$ ratios of $CO_2$ (expressed as $\delta^{13}C$-$CO_2$‰ vs. V-PDB) was carried out with a Finnigan MAT 252 mass spectrometer after standard extraction and purification procedures of the gas mixtures by using liquid $N_2$ and a solid–liquid mixture of liquid $N_2$ and tri-chloroethylene (Evans et al., 1988; Vaselli et al., 2006). Internal (Carrara and San Vincenzo marbles) and international (NBS18 and NBS19) standards were used for estimation of external precision. The analytical error and the reproducibility were ±0.05‰ and ±0.1‰, respectively.

The He isotopic ratios (expressed as R/Ra, where R is the $^3He/^4He$ measured ratio and Ra is the $^3He/^4He$ ratio in the air: $1.39 \times 10^{-6}$; Mamyrin and Tolstikhin, 1984), and the $^4He/^{20}Ne$ ratio were analyzed by separately introducing He and Ne into a split-flight-tube mass spectrometer (GVI Helix SFT) after performing standard purification procedures (e.g., Rizzo et al., 2015). The analytical error was ±1%. In order to minimize isotope fractionation due to He diffusion through the glass flasks (Sano and Fischer, 2013), the He isotope measurements were carried out within a few weeks after sampling. The R/Ra values were corrected for atmospheric contamination based on the $^4He/^{20}Ne$ ratio (Poreda and Craig, 1989), as follows:

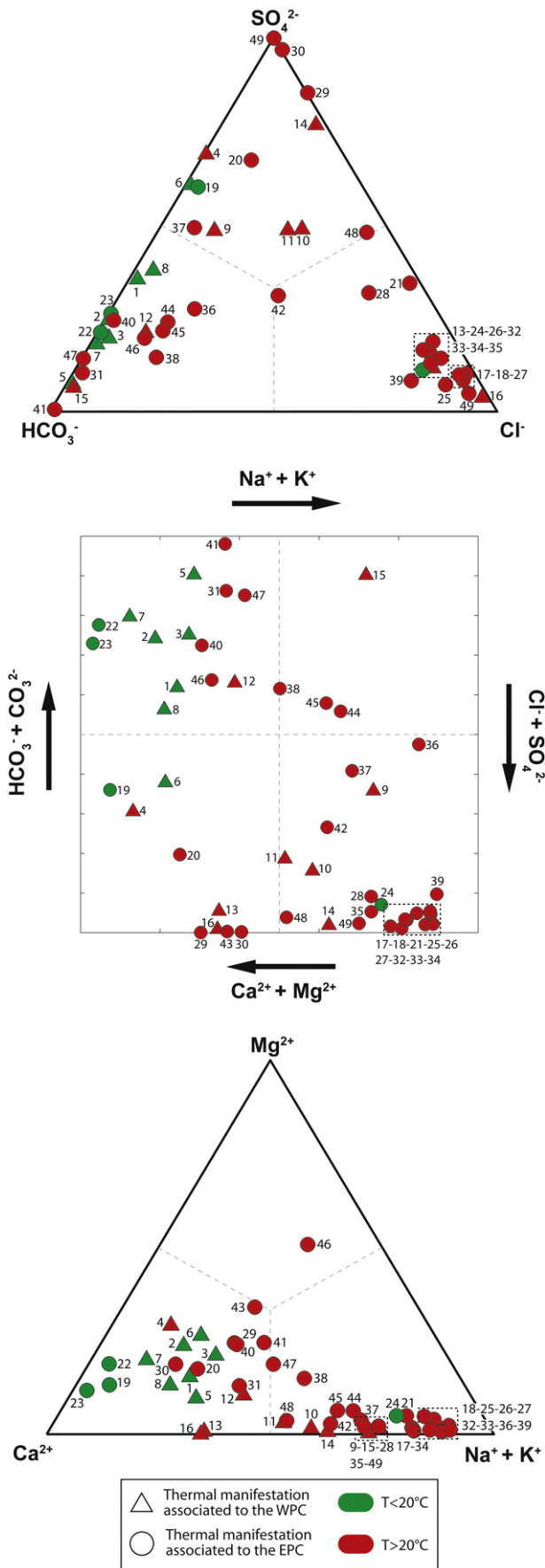$$Rc/Ra = \left[(R/Ra)_{measured} - r\right]/(1-r) \qquad (1)$$

where r = $(^4He/^{20}Ne)_{Air} / (^4He/^{20}Ne)_{measured}$, Rc/Ra is the $^3He/^4He$ ratio normalized to the atmospheric $^3He/^4He$ (Ra) and corrected for air contamination, $(R/Ra)_{measured}$ is the He isotopic ratio measured in the sample and $(^4He/^{20}Ne)_{Air}$ is the atmospheric ratio (0.318; Ozima and Podosek, 1983), while $(^4He/^{20}Ne)_{measured}$ is the ratio measured in the gas sample. A correction of the R/Ra values for the dissolved gases was applied by modifying the $(^4He/^{20}Ne)_{Air}$ values according to the Bunsen solubility coefficients for He and Ne in water. For this study, the solubility coefficients at the water outlet temperature were used. When $(^4He/^{20}Ne)_{measured}$ ~ 1 (e.g. 21a, 24 and 49a have $(4He/^{20}Ne)_{measured}$ ≤ 1.5; Table 3), Rc/Ra values significantly differ with respect to the R/Ra values, whereas for $(^4He/^{20}Ne)_{measured}$ > 1.5Rc/Ra ~ R/Ra independently on the $^4He/^{20}Ne$ value (Air or ASW) used in Eq. (1) (Hilton, 1996).

## 4. Results

### 4.1. Chemical and stable isotopic ($\delta^{18}O$ and $\delta D$) composition of waters

Outlet temperature, pH, total dissolved solids (TDS) values and concentrations of major and minor compounds of 49 waters discharges sampled for this study are reported in Table 1. Six different chemical facies can be recognized (Fig. 3a, b and c), as follows: $Na^+$–$Cl^-$, $Ca^{2+}$–$Cl^-$, $Ca^{2+}$–$HCO_3^-$, $Na^+$–$HCO_3^-$, $Ca^{2+}$–$SO_4^{2-}$ and $Na^+$–$SO_4^{2-}$ (Fig. 3). $Na^+$–$Cl^-$ waters from EPC (17, 18, 21, 24, 25, 26, 27, 28, 32, 33, 34, 35, 39, 42, 48 and 49) were characterized by pH values ranging from 6.2 to 8.6, relatively high TDS values (from 988 to 56,743 mg/L), and temperatures from 6 to 89.4 °C. Similar features characterized the two $Ca^{2+}$–$Cl^-$ waters from WPC (samples 13 and 16), although their $Mg^{2+}$ contents are lower (<2.6 mg/L) when compared to that of the $Na^+$–$Cl^-$ waters with similar $Cl^-$ concentrations (samples 35 and 32; Table 1). The $Ca^{2+}$–$HCO_3^-$ waters from WPC (1, 2, 3, 5, 7, 8 and 12) were cold (T < 20 °C), had pH >7.3 and relatively low TDS (<551 mg/L; Fig. 4). Differently, the $Ca^{2+}$–$HCO_3^-$ waters from EPC (22, 23, 31, 40 and 41) showed relatively wide ranges of TDS (from 584 to 4990 mg/L), temperatures (from 9.1 to 70 °C) and pH values (from 5.4 to 7.5). The $Na^+$–$HCO_3^-$ water (sample 15) from WPC had a low temperature (23.3 °C), TDS (296 mg/L) and high pH (9.2), whereas those from EPC (36, 38,

**Fig. 3.** (a) $HCO_3^-$ $Cl^-$ $SO_4^{2-}$ ternary diagram, (b) square diagram (Langelier and Ludwig, 1942), and (c) $Ca^{2+}$–$(Na^+ + K^+)$–$Mg^{2+}$ ternary diagram for cold and thermal spring from Central Chile. Data are plotted as meq/L.

44, 45, 46 and 47) showed temperatures up to 79.5 °C, slightly acidic to neutral pH (from 5.8 to 7.2), and TDS from 622 to 1648 mg/L (Fig. 4). The $Ca^{2+}$–$SO_4^{2-}$ waters from WPC (samples 4 and 6) had pH ~ 7, relatively low temperatures (<20 °C) and TDS (<698 mg/L), whereas the $Ca^{2+}$–$SO_4^{2-}$ waters from EPC (samples 19, 20, 29, 30 and 43) were acidic (pH ≤ 5.1) and showed TDS values from 449 to 4094 mgL$^{-1}$ and temperatures from 17.8 to 94.5 °C (Fig. 4). The two $Na^+$–$SO_4^{2-}$ waters from WPC (samples 9 and 14) had temperatures up to 33.7 °C, different pH (7.6 and 9.3, respectively) and low TDS (≤338 mg/L), whereas that from EPC (sample 37), showing a similar pH (7.4), had higher temperature and TDS values (46 °C and 930 mg/L, respectively).

Boron concentrations in waters from WPC were relatively low (≤0.6 mg/L) with few exceptions (10, 12, 14 and 17), whereas those from EPC were spanning in a wider range (from 0.03 to 42 mg/L). Lithium concentrations were low in the WPC waters (<1.2 mg/L), whereas those from EPC were strongly enriched (up to 44 mg/L). On the contrary, $NO_3^-$ concentrations were higher in the WPC waters (from 1.5 to 20 mg/L) than in most of those from EPC (<2 mg/L, excepting 17, 20, 21, 24, 25, 26, 27, 34 and 35). Bromide concentrations, ranging from 0.002 to 41 (WPC waters) and from 0.02 to 128 (EPC waters) mg/L, were correlated with those of $Cl^-$.

The $\delta^{18}O$-$H_2O$ and $\delta D$-$H_2O$ values of the WPC waters (Fig. 5), ranging from −7.8 to −12.8‰ and from −50.9 to −91.9‰ vs. V-SMOW, respectively, were distinctly different with respect to those of the EPC waters, whose isotopic intervals were from −11.5 to −15.6‰ and from −83.5 to −107‰ vs. V-SMOW, respectively. Samples 30 (−5.7 and −63‰ vs. V-SMOW, respectively) and 43 (−4.2 and −60.7‰ vs. V-SMOW, respectively) were the only waters from EPC with an isotopic signature similar to that of the WPC waters.

### 4.1. Chemical and stable isotopic ($\delta^{13}C$-$CO_2$) composition of dissolved gases

Outlet temperatures, as well as chemical and $\delta^{13}C$-$CO_2$ values of dissolved gases (only from EPC) are reported in Table 2. Carbon dioxide (from 325 to 772 mmol/mol) and $N_2$ (from 210 to 634 mmol/mol) were the most abundant gas species, whereas $O_2$ varied in a wide range (between 0.32 and 26 mmol/mol). Argon, $CH_4$, $H_2$ and He had concentrations lower than 16, 0.066, 0.039, and 0.0025 mmol/mol, respectively. The $\delta^{13}C$-$CO_2$ values ranged from −14.3 to −6.03‰ vs. V-PDB.

### 4.1. Chemical and stable isotopic ($\delta^{13}C$-$CO_2$, R/Ra, $\delta^{18}O$-$H_2O$ and $\delta D$-$H_2O$) composition of gases from bubbling pools and fumaroles

The chemical and isotopic composition of bubbling gases and fumaroles, which exclusively occur in EPC (Fig. 2a and b), is shown in Table 3. The dry gas fraction of the fumaroles, dominated by water vapor (from 785 to 997 mmol/mol), and the bubbling gases mainly consisted of $CO_2$ (from 628 to 997 mmol/mol) and $N_2$ (from 1.6 to 355 mmol/mol). Bubbling pools from Termas del Flaco (32 and 33) showed $CH_4$ concentrations (up to 6.5 mmol/mol) significantly higher than those measured in the remaining gas samples (≤1.6 mmol/mol). Fumarolic gases, especially those from Baños los Humos (samples 30a, 30b and 30c) and La Plata (samples 50 and 51), had relatively high $H_2$ concentrations (up to 46 mmol/mol) with respect to those of the bubbling pools (≤0.091 mmol/mol). Hydrogen sulfide was detected in the fumarolic gases (from 0.11 to 39 mmol/mol), whereas the bubbling pools were $H_2S$-free. Carbon monoxide (up to 0.0028 mmol/mol) was detected in two fumaroles (samples 39a and 47). Argon and $O_2$ concentrations of the fumaroles (from 0.003 to 0.79 and from 0.003 to 0.16 mmol/mol, respectively) were lower than those of the bubbling pools (from 0.049 to 6.9 and from 0.070 to 9.7 mmol/mol, respectively), whereas the He
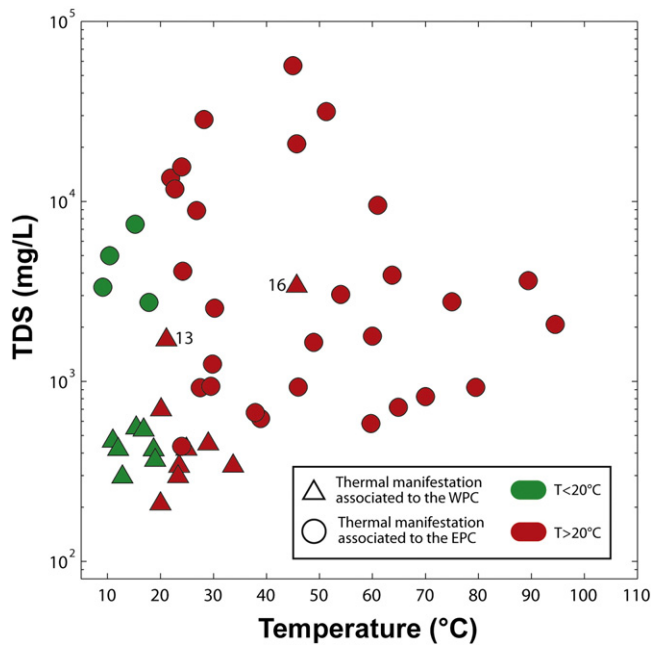
**Fig. 4.** TDS (mg/L) vs. temperature (°C) binary diagram for cold and thermal springs from Central Chile.



**Fig. 5.** δD-H₂O vs. δ¹⁸O-H₂O (‰ vs. V-SMOW) binary diagram for cold and thermal spring from Central Chile. The Local Meteoric Water Line (LMWL; Hoke et al., 2013) is reported.

concentrations of the two types of emergences (<0.041 mmol/mol) did not show significant differences.

The $\delta^{18}O$-H₂O and $\delta D$-H₂O values in the fumarolic steam ranged from −11.9 to −9.4‰ vs. V-SMOW and from −95 to −80‰ vs. V-SMOW, respectively (Fig. 6).

The Rc/Ra values were spanning from 0.47 to 3.90 Ra (Table 3 and Fig. 7), the highest ratios (3.3–3.9) being found in the southern part of EPC, in proximity of Tinguiririca (samples 30b and 30c) and Planchón–Peteroa (samples 50 and 51) volcanic systems and in the Mariposa geothermal area (samples 39a and 47a). The area of San José volcano (sample 52), in the northeastern sector of EPC is characterized by a slightly lower Rc/Ra value (2.91), while Monumento el Morado (sample 22) and Termas del Campanario (sample 49a) bubbling gases were characterized by the lowest Rc/Ra values (0.47 and 0.55, respectively). The $^4He/^{20}Ne$ ratios ranged from 0.8 to 351, i.e. mostly above the atmospheric background ($^4He/^{20}Ne = 0.318$).

The $CO_2/^3He$ ratios vary from 0.42 to 14.6 × 10¹⁰ in the fumaroles, and from 2.9 to 22.2 × 10¹⁰ in the bubbling gases (Fig. 8).

## 5. Discussion

### 5.1. Processes controlling the chemical and isotopic composition of fluid discharges

#### 5.1.1. Water chemistry

The fluid discharges from the two domains (WPC and EPC; Fig. 2a and b) can clearly be distinguished on the basis of their outlet temperatures and TDS values (Fig. 4). With few exceptions (13 and 16), waters from WPC were colder and had lower TDS values with respect to those from EPC. These differences are not surprising, since the occurrence of active volcanic systems and promising geothermal areas in EPC (Fig. 2a) indicate i) an anomalous geothermal gradient (Fig. 2b) favoring water–rock interactions and ii) possible fluid contribution from hot (possibly magmatic) sources. However, the $\delta D$-H₂O vs. $\delta^{18}O$-H₂O diagram in Fig. 5, where the Local Meteoric Water Line (LMWL; Hoke et al., 2013) is also reported, indicates that the aquifers feeding the fluid discharges from both domains had a meteoric origin. Few samples (21, 35, 45 and 46) showed a significant ¹⁸O-depletion likely due to isotopic exchange between liquid water and CO₂ (Epstein and Mayeda,
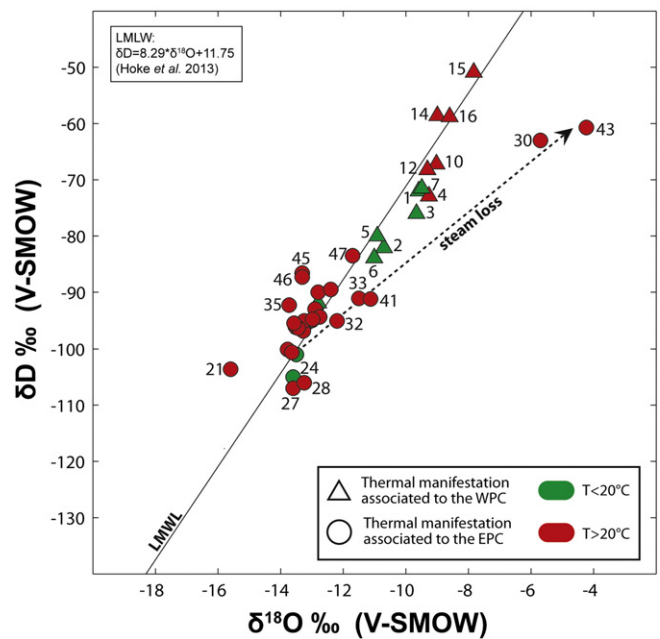
1953), a process that typically affects CO₂-rich bubbling pools (Pauwels et al., 1997) and HCO₃⁻ rich hydrothermal waters (Peiffer et al., 2014). On the contrary, the strong enrichments in both ¹⁸O and ²H shown by samples 30 and 43 were likely due to steam loss through evaporation, favored by the intense bubbling of hot and acidic gases affecting these discharges, as also pointed by the low pH values and $SO_4^{2-}$ dominated composition. A similar process, although occurring at a minor extent, likely caused the isotopic shift shown by other thermal waters from EPC (24, 27, 32, 33 and 41; Fig. 5). However, the relatively high TDS values of these samples (<57,000 mg/L), as well as the elevated heat flow in EPC (<220 mW/m²; Fig. 2b), suggest that their $\delta^{18}O$ enrichment was also produced by prolonged water–rock interactions at temperatures >150 °C (Truesdell and Hulston, 1980).

The WPC waters had higher isotope ratios than those from EPC (Fig. 5) likely due to the difference in altitude of the two domains (Farías et al., 2007), as also highlighted by the altitudes of springs (Table 1). In EPC, both the $Ca^{2+}$–$HCO_3^-$ (31, 40, and 41) and $Na^+$– $HCO_3^-$ (36, 38, 44, 45, 46 and 47) waters located close the volcanic systems (Fig. 2b) showed relatively high temperatures (up to 80 °C) and a slightly acidic to neutral pH. These characteristics are commonly shown by the so-called "peripheral waters" (Giggenbach, 1988, 1991), whose chemistry is produced by prolonged water–rock interaction involving meteoric water and CO₂ fed by the deep source. The largely variable $Ca^{2+}/Na^+$ ratios of these waters were likely dependent on $Ca^{2+}$–$Na^+$ exchange with Na-bearing silicates (e.g. albite) (Marini et al., 2000; Reyes et al., 2010). Relatively large variations of the $HCO_3^-/SO_4^{2-}$ ratios (from 2.5 to 194) were instead produced by different $CO_2/H_2S$ ratios in volcanic/hydrothermal gases interacting with the meteoric aquifer. For instance, at a short distance from the volcanic edifice, where gas discharges showed relatively high H₂S concentrations, $SO_4^{2-}$ dominated and low pH waters were produced (Tupungatito, 19 and 20; Tunguirírica, 29 and 30; Planchón–Peteroa, 43). Thermal waters located close to the Tupungatito volcano (19 and 20) were also affected by $SO_4^{2-}$ and $Ca^{2+}$ contribution from dissolution processes of gypsum occurring in the Mesozoic formations (Fig. 2a), as suggested by their $(Ca^{2+} + Mg^{2+}–HCO_3^-)/SO_4^{2-}$ molar ratios (~1). $Ca^{2+}$–$Na^+$ exchange between rocks and $Ca^{2+}$–$SO_4^{2-}$ waters were likely responsible for the anomalous $Na^+$–$SO_4^{2-}$($HCO_3^-$) composition of sample 37 from the Planchón–Peteroa volcanic system. A similar process can be invoked

**Table 2**

Chemical and stable isotopic ($\delta^{13}$C-$CO_2$; in ‰ vs. V-PDB) composition of dissolved gases from Central Chile. Concentrations are in mmol/mol.

| ID | Name | Date | $CO_2$ | $N_2$ | $CH_4$ | Ar | $O_2$ | $H_2$ | He | $\delta^{13}$C-$CO_2$ |
|----|------|------|--------|-------|--------|-----|-------|-------|-----|------------------------|
| 18 | Salinilla | 2/21/2011 | 466 | 519 | 0.066 | 13 | 2.3 | 0.008 | 0.0025 | −12.6 |
| 19 | Baños Los Azules | 2/21/2011 | 521 | 467 | 0.0020 | 11 | 0.32 | 0.039 | 0.0023 | −10.4 |
| 20 | Termas Tupungato | 2/21/2011 | 772 | 210 | 0.0013 | 4.9 | 13 | 0.022 | 0.0010 | −6.03 |
| 21 | Termas del Plomo 1 | 2/10/2013 | 523 | 444 | 0.010 | 11 | 22 | 0.016 | 0.0015 | −9.19 |
| 26 | Baños Colina | 1/17/2011 | 325 | 634 | 0.0019 | 16 | 26 | 0.015 | 0.0018 | −7.15 |
| 34 | Termas de San Pedro | 3/19/2011 | 356 | 619 | 0.0035 | 15 | 10 | 0.016 | 0.0018 | −14.3 |
| 39 | Barro Colorado 1 | 3/14/2011 | 456 | 523 | 0.0045 | 12 | 8.5 | 0.025 | 0.0017 | −13.4 |

to explain the $Na^+$–$HCO_3^-$ waters. The $Ca^{2+}$–$HCO_3^-$ composition of samples 22 and 23, characterized by a low outlet temperature, pH > 7 and relatively low $HCO_3^-$/$SO_4^{2-}$ ratios (<4.5) was likely related to the interaction between meteoric water enriched in $CO_2$ (Fig. 5) and the Mesozoic formations outcropping in this area (Fig. 2a). The $Na^+$–$Cl^-$ waters (Fig. 3a, b, c) of this domain showed the typical features of mature fluids commonly related to geothermal and volcanic systems (Giggenbach, 1988, 1991): i) relatively high TDS values; ii) high $Li^+$ concentrations (Table 1), dictated by temperature favoring rock leaching by circulating waters (Brondi et al., 1973); iii) high B concentrations (Table 1), favored by circulation of a vapor phase (Giggenbach, 1988, 1991); iv) slightly acidic to neutral pH (Giggenbach, 1988, 1991); and v) relatively low $Cl^-$/$Br^-$ ratios (from 66 to 615), consistent with that (<650) typical of residual brines in geothermal reservoirs (Fontes and Matray, 1993; Davis et al., 2001).

In WPC, most springs (1, 2, 3, 5, 7, 8, 12 and 15) showed the typical features of shallow aquifers fed by meteoric water with no significant fluid contribution from depth (i.e. $HCO_3^-$ dominated composition, not associated with $CO_2$-rich gases, low TDS values, outlet temperatures ≤20 °C and slightly alkaline pH). The origin of such water discharges seems to be related to water–rock interaction processes with the rock formations outcropping in this area mostly consisting of volcanic–volcanoclastic Cenozoic sequences (Fig. 2b). The $Ca^{2+}$–$SO_4^{2-}$ waters (samples 4 and 6) likely derived by dissolution of gypsum/anhydrite-rich layers (Fig. 2a and c), which, coupled with $Ca^{2+}$–$Na^+$ exchange, likely controlled the chemistry of the two thermal springs (9 and 14) showing a $Na^+$–$SO_4^{2-}$ composition. The two $Na^+$–$Cl^-$ waters (10 and 11) were likely originated from the interaction of halide sub-layers occurring within the Mesozoic formations. The uncommon $Ca^{2+}$–$Cl^-$ composition shown by samples 13 and 16 can be hypothesized as the result of an albitization–chloritization affecting basaltic rocks (Hardie, 1983; Mariner et al., 2003), since basaltic to andesitic hydrothermally altered volcanic outcrops, characterized by a secondary mineral assemblage rich in chlorite, chalcedony/quartz and albite formed by partial or complete replacement of primary An-rich plagioclase, were recognized in this area (Vergara et al., 1993; Muñoz et al., 2010). A similar process was invoked to explain the $Ca^{2+}$–$Cl^-$ composition of thermal waters from modern rift zones, oil-field brines and some continental hydrothermal systems (e.g., Reykjanes—Iceland, Salton Sea—USA and Oregon Cascada range—USA; Mariner et al., 2003, and references therein).

### 5.1.2. Chemistry and stable isotopic ratios ($\delta^{13}$C-$CO_2$, R/Ra, $\delta^{18}$O-$H_2O$ and $\delta$D-$H_2O$) of gases

Fumarolic discharges in EPC (Fig. 2b), located in spatial association with volcanoes (30a, b and c: Tinguiririca; 39a: Planchón–Peteroa; 47a: Descabezado Grande–Cerro Azul; 50 and 51: San Pedro–Pellado; 52: San José), showed the typical chemical features of hydrothermal fluids, such as: i) dominant water vapor, ii) variable concentrations of $H_2S$, $CH_4$ and $H_2$, and iii) lack of magmatic gases ($SO_2$, HCl and HF). The $\delta^{18}$O-$H_2O$ and $\delta$D-$H_2O$ values of water vapor of fumaroles (red diamonds; Fig. 6) showed a positive $\delta^{18}$O and $\delta$D shift with respect to the LMWL when considering that recharging meteoric water permeates at ~4000 m a.s.l., i.e. the minimum altitude of the Andes at these latitudes. Since the outlet temperatures of these fluids were at (or slightly above) the boiling point of water at their discharge altitude, their positive

isotope shift (Fig. 6) was likely caused by steam condensation at shallow depth (Stevenson, 1993). According to the Rayleigh model, the isotopic fractionation of vapors affected by condensation can be computed, as follows:

$$\delta = (\delta_i + 1000)F^{\alpha-1} - 1000 \tag{2}$$

where $\delta$ is the delta notation of D/H and $^{18}$O/$^{16}$O of the vapor, F is the vapor fraction after condensation, and $\alpha$ is the liquid–vapor isotope fractionation factor for $^{18}$O–$^{16}$O (1.00509 and 1.00341 at 100 and 200 °C, respectively) and D-H (1.0283 and 1.00237 at 100 and 200 °C, respectively) (Horita and Wesolowski, 1994). As shown in Fig. 6, the fumarolic condensates plot along the line for steam condensation at 100 °C ($S_{100 °C}$ ~ 4.84), i.e. consistent with the outlet temperatures of these discharges.

The Rc/Ra values of the fumarolic discharges were up to 3.90, indicating a contribution of mantle-derived He up to 48%, assuming a three-component mixing model between atmosphere, mantle and crust components having $^3$He/$^4$He ratios of 1 Ra, 8 Ra and 0.02 Ra, respectively (Hilton et al., 2002). Among these gases, San José (sample 52) showed the lowest Rc/Ra value (2.91), corresponding to ~37% of mantle-derived He (%M; Table 3). Bubbling gases displayed Rc/Ra values systematically lower (0.47–2.13; Table 3) than those of the fumarolic gases, evidencing a contribution of mantle-derived He <27%. As shown in Fig. 7, which includes the hydrothermal systems from SVZ (Hilton et al., 1993; Ray et al., 2009; Dobson et al., 2013), the Rc/Ra values of the EPC gases were lower than those shown by fumarolic fluids from active volcanoes in the SVZ, such as the Tupungatito (Tu) (Benavente et al., 2013), Plachón–Peteroa (PP) (Saltori et al., 2012) and Copahue–Caviahue (CC) (Agusto et al., 2013) volcanoes, the latter depicting an increasing trend toward south. This trend seems to reflect the composition of the local magma reservoirs residing in the crust (magma aging), which in the northern zone have higher contents of crustal-derived components (e.g. lower $^3$He/$^4$He and $^{143}$Nd/$^{144}$Nd and higher $^{87}$Sr/$^{86}$Sr ratios) with respect to the magma batches from the southern zone, the latter being enriched in mantle-derived components (e.g. higher $^3$He/$^4$He and $^{143}$Nd/$^{144}$Nd and lower $^{87}$Sr/$^{86}$Sr ratios; Hildreth and Moorbath, 1988). Therefore, the pristine and MORB-like He isotope signature of the mantle source would be lowered by a progressive addition of crust-derived radiogenic $^4$He contamination occurring within magmas residing in the crust to the north. On the basis of these considerations, the low Rc/Ra values measured in EPC gases are related to the mixing, at variable degrees, between a $^3$He-rich end-member from the local magma reservoirs and $^4$He-rich fluids interacting with crustal rocks.

The $\delta^{13}$C-$CO_2$ values measured in fumarole and bubbling gases (from −9.03 to −5.72‰ vs. V-PDB; Table 3) were in the range of mantle $CO_2$ (Rollinson, 1993; Hoefs, 1997; Ohmoto and Goldhaber, 1997), suggesting a dominant contribution of deep-originated compounds. Nevertheless, the high $CO_2$/$^3$He ratios (up to 14.6 × 10$^{10}$; Table 3 and Fig. 8), i.e. up to two orders of magnitude higher than the typical mantle ratio (1.5 × 10$^9$; Sano and Marty, 1995) and up to one order of magnitude higher than the global arc average value (1.2 × 10$^{10}$; Sano and Williams, 1996), imply a significant addition of $CO_2$, which could be produced by both thermometamorphic reactions on limestone and degradation of the organic-rich sedimentary formations of EPC. A

**Table 3**
Chemical and stable isotopic ($\delta^{13}$C-CO$_2$, in ‰ vs. V-PDB; Rc/Ra; R/Ra, $\delta^{18}$O-H$_2$O$_V$ and $\delta$D-H$_2$O$_V$, in ‰ vs. V-SMOW) composition of fumaroles and bubbling gases. $^4$He/$^{20}$Ne, CO$_2$/$^3$He, and CH$_4$/$^3$He ratios, as well as %A, %C and %M values are also reported. Concentrations are in mmol/mol. Geographic coordinates (UTM; WGS-84 19S), altitude (m) and outlet temperature (°C) are also reported.

| ID | Name | type | Date | Cord N | Cord E | Altitude | T°C | CO₂ | H₂S | N₂ | CH₄ | Ar | O₂ | H₂ | He |
|---|---|---|---|---|---|---|---|---|---|---|---|---|---|---|---|
| 21a | Termas del Plomo 2 | Bubbling pool | 2/10/2013 | 6279861 | 415560 | 2962 | 25.2 | 628 | | 355 | 0.146 | 6.9 | 9.7 | | 0.0028 |
| 22 | Monumento el Morado 1 | Bubbling pool | 2/13/2013 | 6260255 | 400543 | 2293 | 9.1 | 956 | | 41 | 0.021 | 0.95 | 1.8 | | 0.0066 |
| 24 | Baños Morales P1 | Bubbling pool | 1/11/2013 | 6256821 | 401927 | 1812 | 15.2 | 892 | | 104 | 0.023 | 2.4 | 1.3 | 0.091 | 0.0026 |
| 27 | Puente de Tierra 1 | Bubbling pool | 2/1/2013 | 6226554 | 404731 | 2148 | 45 | 972 | | 26 | 0.075 | 0.49 | 1.1 | 0.080 | 0.0009 |
| 27a | Puente de Tierra 2 | Bubbling pool | 2/1/2013 | 6226548 | 404754 | 2140 | 44.5 | 965 | | 31 | 0.072 | 0.62 | 3.1 | 0.060 | 0.0011 |
| 30a | Baños Los Humos 2 | Fumarole | 1/25/2013 | 6143073 | 371828 | 2981 | 90.6 | 925 | 0.11 | 35 | 0.066 | 0.15 | 0.090 | 40 | 0.0015 |
| 30b | Baños Los Humos 3 | Fumarole | 1/25/2013 | 6143235 | 371802 | 2976 | 90 | 929 | 0.13 | 26 | 0.058 | 0.12 | 0.050 | 45 | 0.0026 |
| 30c | Baños Los Humos 4 | Fumarole | 1/25/2013 | 6142687 | 371534 | 2879 | 90.7 | 922 | 0.14 | 31 | 0.047 | 0.18 | 0.16 | 46 | 0.0017 |
| 32 | Termas del Flaco 1 | Bubbling pool | 3/25/2012 | 6130555 | 368978 | 1806 | 63.7 | 988 | | 7.7 | 4.6 | 0.061 | 0.095 | 0.0019 | 0.014 |
| 33 | Termas del Flaco 2 | Bubbling pool | 3/25/2012 | 6130555 | 368996 | 1732 | 89.4 | 984 | | 8.9 | 6.5 | 0.049 | 0.11 | 0.0021 | 0.012 |
| 39a | Barro Colorado 2 | Fumarole | 3/14/2011 | 6079574 | 361772 | 2282 | 94.4 | 997 | 0.32 | 1.6 | 0.57 | 0.003 | 0.034 | 0.11 | 0.0015 |
| 47a | Estero del Volcán 2 | Fumarole | 1/15/2012 | 6070452 | 339996 | 1960 | 112 | 989 | 4.6 | 6.2 | 0.14 | 0.011 | 0.025 | 0.11 | 0.0058 |
| 49 | Termas del Campanario 1 | Bubbling pool | 2/15/2013 | 6022199 | 356881 | 1545 | 45.7 | 754 | | 234 | 0.20 | 5.2 | 6.9 | | 0.0049 |
| 49a | Termas del Campanario 2 | Bubbling pool | 2/15/2013 | 6022198 | 356923 | 1544 | 38.5 | 734 | | 255 | 0.26 | 4.6 | 5.9 | | 0.0045 |
| 50 | La Plata 1 | Fumarole | 2/16/2013 | 6019525 | 344668 | 1953 | 94.3 | 901 | 25 | 62 | 1.6 | 0.79 | 0.004 | 9.3 | 0.041 |
| 51 | La Plata 2 | Fumarole | 2/16/2013 | 6019548 | 344296 | 2183 | 93 | 902 | 39 | 34 | 1.0 | 0.54 | 0.003 | 23 | 0.041 |
| 52 | San Josè | Fumarole | 2/2/2012 | 6261279 | 416255 | 5756 | 81.4 | 991 | | 8.5 | 0.017 | 0.14 | 0.14 | 0.016 | 0.011 |

significant crustal carbon source related to both biogenic and thermogenic processes is supported by the CH$_4$/$^3$He ratios (up to 83.3 × 10$^6$; Table 3), which are higher than those measured in sediment-free mid-ocean ridge (<1 × 10$^5$; Snyder et al., 2003). In order to test this hypothesis and according to the approach proposed by Sano and Marty (1995), the relative contribution of carbon from mantle degassing (M), limestone (L) and/or organic-rich sediments (S) can be calculated, as follows:

$$M + S + L = 1 \tag{3}$$

$$\left(\delta^{13}C - CO_2\right)_{meas} = M\left(\delta^{13}C - CO_2\right)_{MORB} + L\left(\delta^{13}C - CO_2\right)_{Lim} + S\left(\delta^{13}C - CO_2\right)_{sed} \tag{4}$$

$$\left[1/(CO_2/^3He)\right]_{meas} = \left[M/(CO_2/^3He)\right]_{MORB} + \left[L/(CO_2/^3He)\right]_{Lim} + \left[S/(CO_2/^3He)\right]_{Sed}. \tag{5}$$

Calculations of the M, S and L fractions (in %; Table 3) were carried out considering the following end-members: $(\delta^{13}C\text{-}CO_2)_{MORB} = -6.5$‰, $(\delta^{13}C\text{-}CO_2)_{Sed} = -30$‰, $(\delta^{13}C\text{-}CO_2)_{Lim} = 0$‰, $(CO_2/^3He)_{MORB} = 1.5 \times 10^9$, $(CO_2/^3He)_{Sed} = 1 \times 10^{13}$ and $(CO_2/^3He)_{Lim} = 1 \times 10^{13}$. These results confirm a low mantle CO$_2$ fraction (M < 4.1%), whereas limestone was largely the most abundant crustal carbon source (L and S up to 73.3 and 32.4%, respectively). This means that contributions from the subducting slabs and the sedimentary basement controlled the budget of CO$_2$ [(L + S) / M up to 150], as already observed by Ray et al. (2009) in other geothermal areas of SVZ and by Benavente et al. (2013) at the Tupungatito volcano. Mixing between limestone (L) and/or organic-rich sediments (S), at comparable mantle contribution, could also have produced such strong variations of the $\delta^{13}$C-CO$_2$ values. Most data indeed fall indeed within an area limited by two hypothetical mixing lines between M and two possible end-members with 27% and 37% of organic carbon added to limestone (Fig. 8). The lowest $\delta^{13}$C-CO$_2$ values measured in samples 22 and 49a, which also showed the lowest Rc/Ra values of our dataset, are in accordance with the latter inference, being these gases characterized by the highest percentages of organic-rich sedimentary CO$_2$ (S = 32.4 and 36.8, respectively). Samples 50 and 51 are the only exceptions, since they were characterized by relatively high M fraction (31.9 and 35.7%). This evidence is in contrast with the Rc/Ra (3.4 and 3.8) and $\delta^{13}$C-CO$_2$ (−8.9 and −8.1‰ vs. V-PDB, respectively) values of these samples, which were comparable to those measured in other samples (i.e., 30b, 30c and 47a). It is worth noting that the high %M values of samples 50 and 51 were due to their low

CO$_2$/$^3$He ratios, which were the lowest of our dataset and even lower than the global arc average value (1.2 × 10$^{10}$). Such relatively low CO$_2$/$^3$He ratios can be produced by a secondary process according to which a selective dissolution in water of CO$_2$ with respect to the less soluble species (e.g. Ray et al., 2009) occurred, as suggested by relatively high He, CH$_4$ and Ar concentrations shown by these gases (Table 3). To investigate the effect of preferential loss of CO$_2$ into a liquid phase on the measured CO$_2$/$^3$He ratios, the Rayleigh fractionation model was applied, as follows:

$$r_{be} = r_{af} F^{(\alpha - 1)} \tag{6}$$

where $r_{be}$ and $r_{af}$ represent the CO$_2$/$^3$He ratios after and before gas removal respectively, 'F' is the fraction of gas remaining after gas removal, and $\alpha$ is the fractionation factor expressed as the ratio of CO$_2$ and He solubilities (S) in water (S$_{CO2}$/S$_{He}$ = 61.4499 at 40 °C, 33.4724 at 70 °C, and 10.5094 at 160 °C; Taran, 2005). Assuming an initial CO$_2$/$^3$He value of 6.6 × 10$^{10}$, i.e. the ratio of the fumarole with the highest Rc/Ra value (sample 30b), the measured CO$_2$/$^3$He ratio in sample 51 would require a gas loss (1 − F) of ~4%, 8% and 25% at 40°, 70° and 160 °C, respectively. It is worth noting that samples 30b, 50 and 51 had comparable $\delta^{13}$C-CO$_2$ values. Thus, CO$_2$ associated with these waters was not affected by isotopic fractionation, likely because its dissolution occurred at T > 125 °C (Mook et al., 1974).

As shown in the N$_2$–He–Ar ternary diagram (Giggenbach, 1992; Fig. 9), fumarolic discharges from the surroundings of Tinguiririca (30a, b and c), Planchón–Peteroa (39a) and Descabezado Grande–Cerro Azul (47a) volcanoes were characterized by N$_2$/Ar ratios >84 (air value), typically shown by arc-type gases (Giggenbach, 1992). Samples from San Pedro–Pellado (50 and 51) and San José (52) volcanoes, showed relatively low N$_2$/Ar ratios (<84) likely due to mixing processes between gases from ASW (N$_2$/Ar ~ 38) and a less evolved, He-rich magma source. This hypothesis is consistent with the high calculated %M values of these samples (6.8% to 35.7%; Table 3). Bubbling gases located 16 km south of Tinguiririca volcano (32 and 33) were characterized by higher He contents (and similar N$_2$/Ar ratios) than those determined in the fumaroles located at the summit craters (30a, b and c) (Fig. 9). Such a He-excess was likely produced by (i) CO$_2$ dissolution related to the occurrence of an aquifer at the base of the volcano, and (ii) $^4$He addition due to water–rock interactions typically affecting gas discharges at the periphery of hydrothermal-dominated volcanic systems. The latter process is also supported by the relatively low Rc/Ra value of the bubbling gases (2.13) with respect to those of the fumaroles (3.6 and 3.9). The relatively low $^4$He/$^{20}$Ne ratios (≤8.5; Table 3) shown by

| CO | H$_2$O | R/Ra | $^4$He/$^{20}$Ne | Rc/Ra | %A | %C | %M | δ$^{13}$C-CO$_2$ | δD-H$_2$O | δ$^{18}$O-H$_2$O | CO$_2$/$^3$He (10$^{10}$) | CH$_4$/$^3$He (10$^6$) | M | L | S |
|---|---|---|---|---|---|---|---|---|---|---|---|---|---|---|---|
| | | 1.05 | 0.8 | 1.07 | 39.7 | 51.9 | 8.4 | −7.76 | | | 15.1 | 35.1 | 0.98 | 73.3 | 25.7 |
| | | 0.49 | 8.5 | 0.47 | 3.7 | 90.1 | 6.2 | −9.76 | | | 22.2 | 4.9 | 0.66 | 67.0 | 32.4 |
| | | 1.53 | 0.9 | 1.81 | 35.3 | 49.7 | 14.9 | −8.60 | | | 13.8 | 3.5 | 1.07 | 70.5 | 28.5 |
| | | | | | | | | −10.9 | | | | | | | |
| | 956 | | | | | | | −8.90 | −88 | −11.2 | | | | | |
| | 944 | 3.85 | 17 | 3.90 | 1.8 | 50.0 | 48.2 | −8.50 | −85 | −10.8 | 6.6 | 4.1 | 2.26 | 69.8 | 27.9 |
| | 966 | 3.58 | 38 | 3.60 | 0.8 | 54.2 | 45.0 | −8.70 | −87 | −11.0 | 10.8 | 5.5 | 1.37 | 69.9 | 28.7 |
| | | | | | | | | −9.77 | | | | | | | |
| | | 2.12 | 47 | 2.13 | 0.6 | 72.5 | 26.8 | −8.34 | | | 2.9 | 190 | 5.16 | 67.9 | 26.9 |
| 0.0028 | 827 | 3.26 | 56 | 3.27 | 0.5 | 58.4 | 41.0 | −5.72 | −89 | −11.1 | 14.6 | 83.3 | 1.01 | 80.1 | 18.9 |
| 0.0018 | 882 | 3.40 | 351 | 3.40 | 0.1 | 57.1 | 42.8 | −8.12 | −80 | −9.4 | 3.6 | 5.1 | 4.15 | 69.5 | 26.3 |
| | | | | | | | | −11.1 | | | | | | | |
| | | 0.65 | 1.5 | 0.55 | 21.2 | 73.0 | 5.8 | −11.1 | | | 21.3 | 75 | 0.69 | 62.5 | 36.8 |
| | 882 | 3.39 | 70 | 3.40 | 0.4 | 56.9 | 42.7 | −8.90 | −80 | −9.4 | 0.47 | 8.3 | 31.9 | 43.8 | 24.3 |
| | 997 | 3.79 | 86 | 3.80 | 0.3 | 52.0 | 47.6 | −8.10 | −93 | −11.8 | 0.42 | 4.6 | 35.7 | 43.3 | 21.0 |
| | 785 | 2.90 | 95 | 2.91 | 0.3 | 63.1 | 36.6 | −9.03 | −95 | −11.9 | 2.2 | 0.38 | 6.8 | 64.3 | 28.9 |

the other bubbling gases seem to imply a significant contamination of atmospheric He, as also suggested by the relative proportion of N$_2$–Ar–He (Fig. 9).

### 5.1.3. Chemical equilibria in the liquid phase

With the aim to investigate the chemical–physical conditions dominating the source regions of hydrothermal fluids feeding the thermal springs in the whole investigated area, a theoretical approach based on the equilibria of chemical reactions involving ionic species of water and different mineral phases, was carried out in this section. Equilibrium temperatures of hydrothermal reservoirs are commonly evaluated on the basis of the equilibrium reactions in the Na$^+$–K$^+$–Mg$^{2+}$–Ca$^{2+}$ system (Fournier and Truesdell, 1973; Fournier and Potter, 1978; Fournier, 1979; Giggenbach, 1988, 1991). As shown in the Na/400–K/10–√Mg ternary diagram (Fig. 10), where the fields of "fully equilibrated", "partially equilibrated" and "immature" waters were obtained by combining the fast responding K–Mg geothermometer with the slowly re-equilibrating Na–K geothermometer (Giggenbach, 1988), cold waters are confirmed to be strongly immature. The only exception (partial equilibrium at T ~ 170 °C) was represented by sample 24 from EPC, a Na$^+$–Cl$^-$ water with relatively high TDS value (~7000 mg/L). A group of waters defines a dilution trend (A) from the partial equilibrium field at temperatures ranging from 200 to 240 °C (28, 32, 33, 34, 39 and 49) to the Mg corner (20, 35, 38, 41, 42, 43, 46 and 48). A second dilution trend (B) at lower temperatures (from 120 to 160 °C) is depicted by samples 16, 17, 24, 25, 26 and 27 (at partial equilibrium) and samples 15, 36, 37, 44 and 45 (in the immature field). A third, low temperature (<100 °C) trend (C) includes samples 9, 10, 11, 13, 18 and 21. Waters that tend to full equilibrium along the trend (A) are from EPC and had a Na$^+$–Cl$^-$ composition and relatively high TDS values (Table 1), i.e. the typical features of mature waters related to the active volcanoes (Giggenbach, 1988). Differently, partial equilibrium of trends B and C includes both Na$^+$–Cl$^-$ waters from EPC (21, 24, 25, 26 and 27) and waters far from the active volcanic chain (17 and 18). Therefore, it cannot be excluded that the latter waters were affected by some addition of the Na$^+$–Cl$^-$ brine uprising from the eastern deep systems through west-verging thrust faults (Farías et al., 2010; Giambiagi et al., 2014) (Fig. 2b). This hypothesis is also supported by the presence of significant amounts of mantle He (19%) as dissolved phase in sample 17 (R/Ra ~ 1.56; Hilton et al., 1993).

The increasing Mg$^{2+}$ concentrations of the Na$^+$–Cl$^-$ waters along both the A and B trends (Fig. 10) correspond to decreasing TDS values (Table 1), thus they were likely produced by dilution of mature, volcanic/geothermal brines. The apparent partial equilibrium attained

by the WPC waters on the B and C trends was unlikely. In fact, samples 9, 10 and 11 had low TDS values, whereas the Ca$^{2+}$–Cl$^-$ composition of samples 13 and 16 was likely due to albitization–chloritization of basalts, which is not consistent with the paragenesis at the basis of the Na$^+$–K$^+$–Mg$^{2+}$ geothermometer.

In the (10K / [10K + Na] vs. 10Mg / [10Mg + Ca]) diagram (Fig. 11) those waters from EPC showing some degree of attainment of equilibrium in Fig. 10 are reported. All samples plot far from the equilibrium curve proposed by Giggenbach (1988), suggesting that the EPC waters approached their equilibrium with rocks characterized by a mineral assemblage different with respect to that used to construct the original diagram. The EPC basement is characterized by carbonate–evaporite rocks, consequently a mineral assemblage involving calcite, dolomite, anhydrite and fluorite (e.g. Marini et al., 1986) is expected to be the most appropriate to describe water–rock interactions in this area. According to Chiodini et al. (1995), chemical equilibrium in the Ca$^{2+}$–Mg$^{2+}$–H$_2$O system is given by the following equation:

$$\log\left(Ca^{2+}/Mg^{2+}\right) = 3.117 - 979.8/(T + 273.15) + 0.03904 \\ * \log(P_{CO2}) + 0.07003 * \log(\Sigma_{eq}) \tag{7}$$

where T is the temperature (in °C), P$_{CO2}$ is the partial pressure of CO$_2$ (in bar) and $\Sigma_{eq}$ is the salinity of the solution (in mol/L). On the other hand, the Na$^+$–K$^+$ ratios of these waters were likely controlled by the cation exchange between Na- and K-feldspars (Fig. 10), whose dependence on the temperature can be computed according to the following equation (Giggenbach, 1988):

$$\log(K^+/Na^+) = 1.75 - [1390/(T + 273.15)] \tag{8}$$

Samples 24, 25, 26, 27, 34 and 39 plot close to the equilibrium lines (green and blue dotted curve) constructed considering P$_{CO2}$ values of 0.1, 1, 10 and 100 bar, $\Sigma_{eq}$ values in the range of these samples (from 0.02 to 2 eq/L), and temperatures from 60 to ~300 °C (Fig. 11). However, most Na$^+$–Cl$^-$ samples plot at unrealistic high $\Sigma_{eq}$ and P$_{CO2}$ values (>20 eq/L and/or >100 bar, respectively), suggesting that the chemistry of these waters was controlled by a different mineral paragenesis. Chemical equilibria albite, K-feldspar, Ca- and Mg-saponite, the two clay-minerals being typically involved in rock–water interactions producing "mature" waters and recognized in the drilling logs wells at the Tinguiririca geothermal field (Droguett et al., 2012), can be
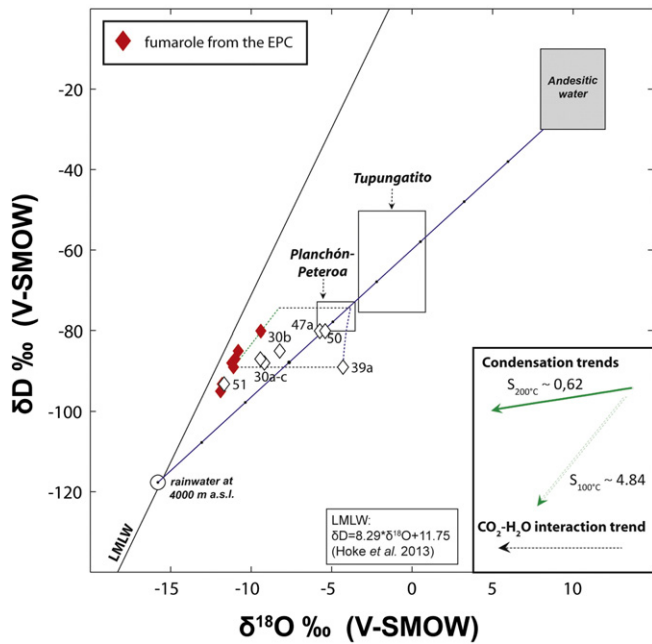
**Fig. 6.** δD-$H_2O$ vs. δ$^{18}$O-$H_2O$ (‰ vs. V-SMOW) binary diagram for fumarolic steam from Central Chile. The Local Meteoric Water Line (LMWL; Hoke et al., 2013) and the field of "Andesitic water" (Taran et al., 1989) are reported. White diamonds: calculated isotopic composition of fumaroles prior to condensations (details are reported in the text).

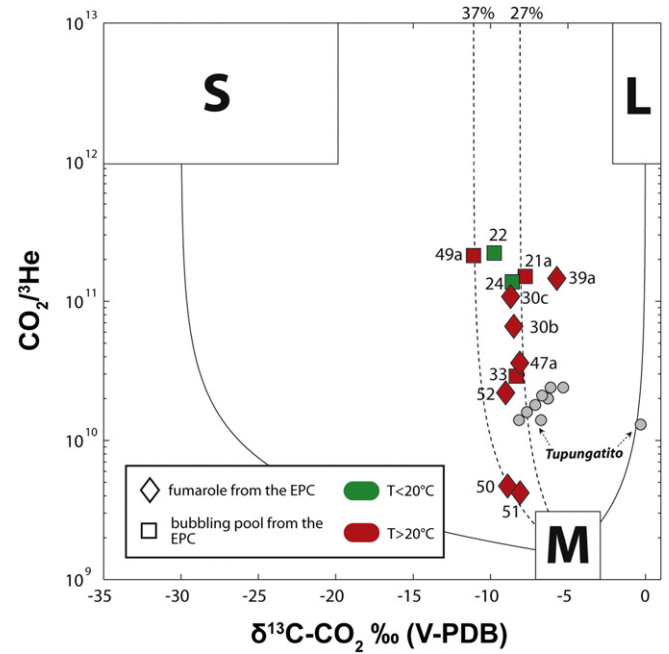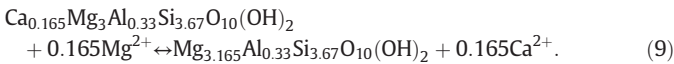calculated using Eq. (8) and the chemical reaction between Ca- and Mg-saponite, as follows:

$$Ca_{0.165}Mg_3Al_{0.33}Si_{3.67}O_{10}(OH)_2 \\ + 0.165Mg^{2+} \leftrightarrow Mg_{3.165}Al_{0.33}Si_{3.67}O_{10}(OH)_2 + 0.165Ca^{2+}. \tag{9}$$



**Fig. 8.** $CO_2$/$^3$He vs. δ$^{13}$C-$CO_2$ binary diagram. End-member compositions of sedimentary (organic)-derived carbon (S), calcareous (limestone)-derived carbon (L) and mantle-derived carbon (M) are from Sano and Marty (1995). Binary mixing curves between S and M, between L and M, and between S and L (solid lines) are reported. Dotted lines represent binary mixing between M and two possible end-members with 27% and 37% of organic carbon added to limestone.

Assuming that the activity ratios for the saponite solid mixture are close to unity (Giggenbach, 1988; Marini, 2006) and that the activity coefficients of bivalent cations are similar (i.e., $\gamma Ca^{2+} \sim \gamma Mg^{2+}$), the $Ca^{2+}$/$Mg^{2+}$ (in mg/kg) ratios can be calculated using the
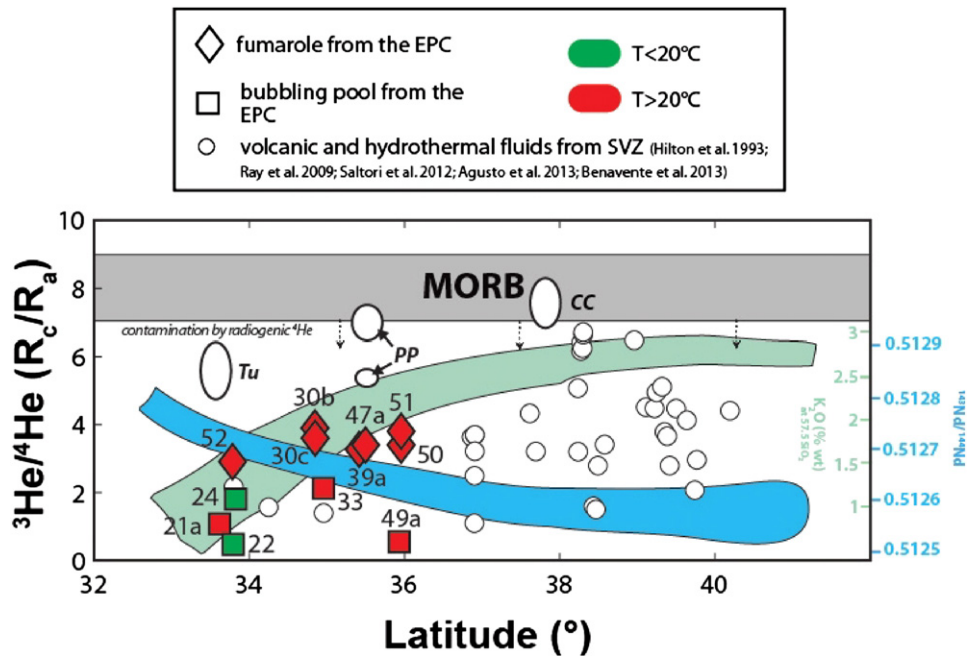


**Fig. 7.** $^3$He/$^4$He ratios (expressed as Rc/Ra) vs. Latitude binary diagram. Fumarolic gases from the Tupungatito (Tu), Planchón–Peteroa (PP) and Copahue–Caviahue (CC) volcanoes and other hydrothermal fluids from SVZ (Hilton et al., 1993; Ray et al., 2009; Saltori et al., 2012; Agusto et al., 2013; Benavente et al., 2013) are reported for comparison. The $K_2O$ contents (green area) and $^{143}$Nd/$^{144}$Nd ratios (blue area) of volcanic rocks along the SVZ are also reported for comparison (Hildreth and Moorbath, 1988). Along-arc variations in chemical and isotopic composition of volcanic rocks from the SVZ indicate an increasing participation of continental crust in the magma genesis to the north (Hildreth and Moorbath, 1988; Cembrano and Lara, 2009). (For interpretation of the references to color in this figure legend, the reader is referred to the web version of this article.)
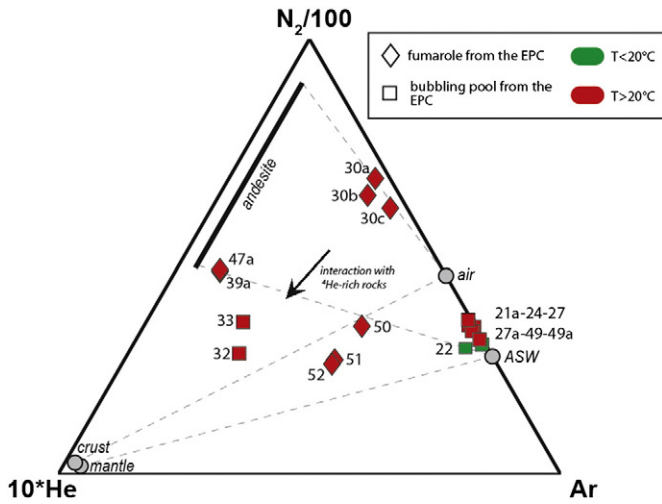
Fig. 9. $N_2$–Ar–He ternary diagram (Giggenbach, 1992) for fumaroles and bubbling gases from Central Chile.

following temperature-dependent relations (T in °C) computed using the thermodynamic data from Delany and Lundeen (1991):

$$\log\left(Ca^{2+}/Mg^{2+}\right) = 0.0356 + 0.012T - 4.121\left(T^2/10^5\right) \\ + 0.848\left(T^3/10^7\right) - 0.569\left(T^4/10^{10}\right) \quad (10)$$

As shown in Fig. 11, the $Na^+$–$Cl^-$ waters seem to have attained chemical equilibria in the $Na^+$–$K^+$–$Ca^{2+}$–$Mg^{2+}$ system at temperatures consistent with those indicated by the Na/400–K/10–√Mg ternary diagram (Fig. 10), in presence of the mineral paragenesis considered to compute Eqs. (7), (8) and (10), i.e. calcite, dolomite, anhydrite, fluorite, albite, K-feldspar, Ca- and Mg-saponite. It is worth noting that the temperatures estimated for the $Na^+$–$Cl^-$ waters from Tinguiririca volcano (32, 33 and 34: >230 °C) and the San Pedro–Pellado volcanoes (48 and 49: ~200 °C) are in good agreement with those measured at the bottom of the slim holes drilled in these systems (Clavero et al., 2011; Hickson et al., 2011).

As suggested by Chiodini et al. (1995), equilibrium temperatures of $Ca^{2+}$–$SO_4^{2-}$, $Na^+$–$SO_4^{2-}$, and $Na^+$–$HCO_3^-$ springs from WPC and EPC, i.e. those likely controlled by the interaction with the Mesozoic carbonate–gypsum formations with no significant contribution from the $Na^+$–
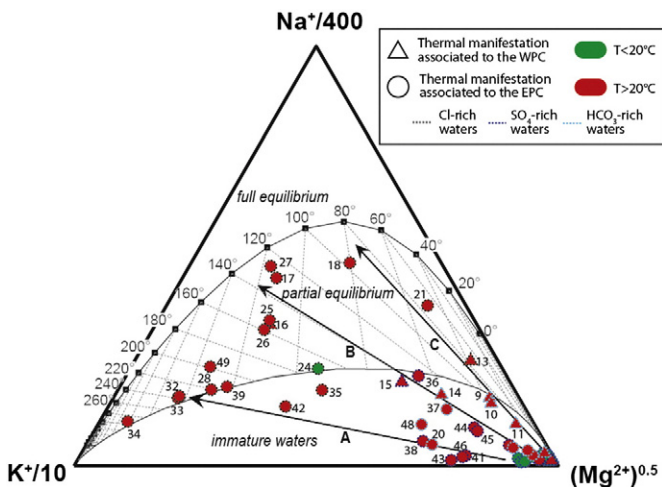
$Cl^-$ brine, can be conveniently computed considering the theoretical concentrations of $HCO_3^-$, $SO_4^{2-}$ and $F^-$ in equilibrium with calcite, dolomite, anhydrite and fluorite. The theoretical T-$P_{CO2}$ grid in the $SO_4^{2-}$-$F^-$-$HCO_3^-$ ternary diagram (Fig. 12) was calculated for salinities (0.02 and 0.5 mol/L) consistent with those of the plotted waters. Thermal waters from the southern sector of EPC close to the Planchón–Peteroa and Descabezado Grande–Cerro Azul volcanoes (36, 37, 38, 44, 45 and 47) seem to have attained equilibrium at temperatures from 105 to 150 °C and $P_{CO2}$ values from 1 to 10 bars. On the contrary, the two thermal $Ca^{2+}$–$SO_4^{2-}$ waters from the northern end of EPC (19 and 20) and those from WPC (4, 6, 9 and 14) plot at relatively low equilibrium temperatures (<55 °C) and $P_{CO2}$ values indicating a shallow and cooler hydrological pattern.

### 5.1.4. Chemical equilibria in the gas phase

Among $H_2O$–$H_2$–$CO$–$CO_2$–$CH_4$, i.e. the main gas compounds sensitive to changes of chemical–physical conditions in hydrothermal systems, $H_2O$ and $CO$ cannot reliably be used for geothermometric purposes to the gas discharges investigated in the present study. These two compounds are indeed strongly dependent on steam condensation processes due to the presence of liquid water at various temperatures at the surface (bubbling pools) and also affecting the fumarolic discharges (Fig. 6). Therefore, fluid reservoir temperatures can be preferably investigated using the $CO_2$ geothermometer proposed by Giggenbach and Goguel (1989), which assumes that $P_{CO2}$ is controlled by interactions with crustal rocks. Another geothermometer that can be usefully be applied to hydrothermal fluids is based on the dependence on temperature of $H_2$ fugacity (Giggenbach, 1987). Problems related to the use of the univariant reactions involving these two sensitive species can be prevented by formulating isomolar concentration ratios with a chemically inert constituent, such as Ar that is assumed to have a meteoric origin in hydrothermal reservoirs (Giggenbach, 1991).

Considering that hydrothermal fluids are $O_2$-free, to avoid the effect of possible atmospheric contamination at the surface, Ar concentrations were transformed into Ar* values, as follows:

$$Ar_* = Ar - O_2/22 \quad (11)$$

where the $O_2/22$ ratio represents a minimum estimation (being $O_2$ rapidly consumed by redox reactions) of the Ar concentration from



Fig. 10. Na–K–Mg ternary diagram proposed by Giggenbach (1988) for thermal and cold springs from Central Chile. The axes (Na/400–K/10–√Mg) were modified to enlarge the low temperature area of the diagram.
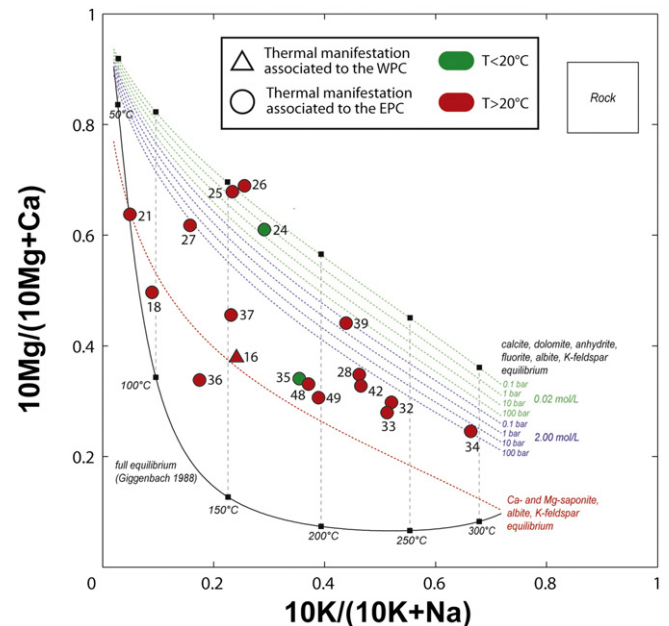


Fig. 11. (10K/[10K + Na] vs. 10Mg/[10Mg + Ca]) binary diagram (Giggenbach, 1988) for thermal and cold springs from Central Chile.
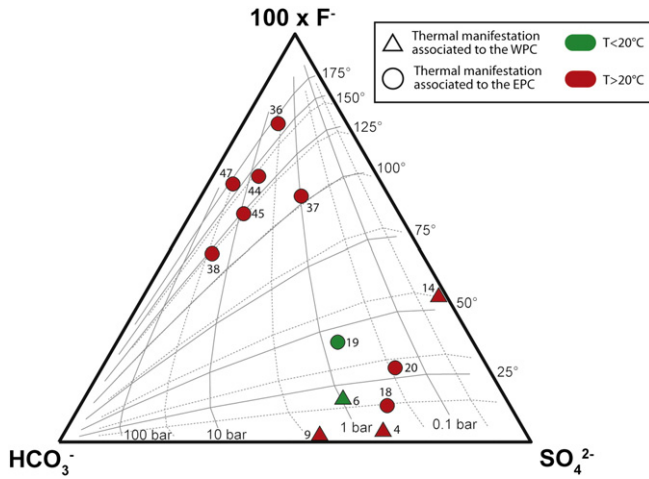
Fig. 12. $SO_4^{2-}$–$F^-$–$HCO_3^-$ ternary diagram (Marini et al., 1986; Chiodini et al., 1995) for thermal and cold springs from Central Chile. Two theoretical T–$P_{CO_2}$ grids for salinities of 0.02 mol/L (solid lines) and 0.5 mol/L (dotted lines) are shown.

atmospheric contamination. The dependences of $H_2$ on $R_H$ in the two phases can be expressed, as follows:

$$\log(H_2/Ar*)_V = R_H + 6.52 \tag{12}$$

$$\log(H_2/Ar*)_L = R_H - \log(B_{H2}) + 6.52 \tag{13}$$

where $B_{H2}$ is the vapor/liquid distribution coefficients of $H_2$. At redox conditions controlled by the $Fe^{II}$–$Fe^{III}$ (GT) redox buffer system [RH = $\log(H_2/H_2O) = -2.8$; Giggenbach, 1987], the dependence of $CO_2/Ar*$ ratios on temperature is given by:

$$\log(CO_2/Ar*)_V = -2.81 - 5012.7/T - 0.00919 \times T + 6.464 \times \log(T) \tag{14}$$

$$\log(CO_2/Ar*)_L = -2.81 - 5012.7/T - 0.00919 \times T + 6.464 \times \log(T) - \log(B_{CO2}) \tag{15}$$

where T is in K and $B_{CO2}$ is the vapor/liquid distribution coefficient of $CO_2$. The combination of the $CO_2/Ar*$ and $H_2/Ar*$ geothermometers from 150 to 350 °C was graphically displayed in Fig. 13. Fumarolic gases from the Tinguiririca (30a, b, c) and the San Pedro–Pellado volcanoes (50 and 51) approached equilibrium in a vapor phase separated from a liquid at 200–250 °C. This temperature range is consistent with that attained by the liquid phase of the thermal waters from those areas (32–33 and 49, respectively; Figs. 10 and 11). Nevertheless, the bubbling gases from the same areas were far from the equilibrium (Fig. 13), possibly due to (i) $H_2$ consumption and/or (ii) Ar addition, both likely occurring at shallow depth in the bubbling water. Similar processes can also have affected the other bubbling gases (24, 27 and 27a; Fig. 13), especially those having no detectable $H_2$ concentrations (21a, 22, 49 and 49a; Table 3), and the fumarole from San José volcano (52). Fumaroles from Planchón–Peteroa (39a) and Descabezado Grande–Cerro Azul (47a) areas seem to have attained equilibrium in the liquid phase at relatively high temperature (>300 °C). Accordingly, in these gases CO was measured at significant concentrations (Table 3). However, the thermal waters associated with these systems were mostly immature or approach equilibrium at temperatures <210 °C (Figs. 10 and 11). This suggests the occurrence of high-temperature fluids whose liquid phase was partially diluted by shallow aquifers, whereas the gas fraction maintained the composition acquired at depth.

Chemical reactions involving $CH_4$ are kinetically slow, thus they can provide information about the equilibria attained at deeper levels with
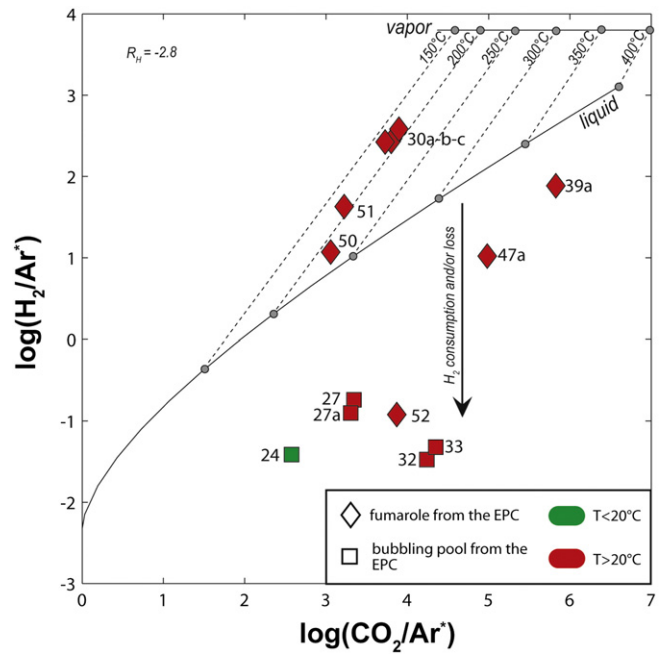


Fig. 13. Log($H_2$/*Ar) vs. log($CO_2$/*Ar) binary diagram for bubbling and fumarolic gases from Central Chile. Solid lines refer to equilbria in the vapor and liquid phases controlled by the GT redox buffer system at temperatures from 150 to 350 °C (Giggenbach, 1987).

respect to the quick responding geothermometers (Giggenbach, 1987, 1991; Chiodini and Marini, 1998). Assuming that the $CH_4$–$CO_2$ pair is regulated by the Sabatier reaction ($CH_4 + 2H_2O \leftrightarrow CO_2 + 4H_2$) and that $\log fH_2O = 4.9 - 1820 / T$ (Giggenbach, 1987), the dependence of the $\log(CO_2/CH_4)$ values on temperature and $R_H$ in the vapor and the liquid phases is, as follows:

$$\log(CH_4/CO_2)_V = 4 R_H + 5181/T(K) \tag{16}$$

$$\log(CH_4/CO_2)_L = 4 R_H + 5181/T(K) + \log(B_{CO2}) - \log(B_{CH4}). \tag{17}$$

Eqs. (12), (13), (16) and (17) were used to construct the T–$R_H$ grid in the $CO_2$–$CH_4$–$H_2$ system that is reported in the log($X_{H2}/X_{Ar*}$) vs. log($X_{CH4}/X_{CO2}$) diagram (Fig. 14). As expected, the $CO_2$–$CH_4$–$H_2$ equilibrium temperatures of the Tinguiririca and San Pedro–Pellado fumaroles (30a–b–c, 50 and 51) are significantly higher (up 350 °C) with respect to those estimated by the $CO_2$–$H_2$ geothermometer. The apparent low equilibrium temperatures (<150 °C) and highly oxidizing conditions ($R_H < -3.4$) of fluids from the Tinguiririca bubbling pools (32 and 33) were likely caused by $H_2$-consumption, as also evidenced in Fig. 13. Similarly, the relatively low $H_2$ (Fig. 13) and $CH_4$ (Fig. 14) contents of the other bubbling gases and the San José fumarole (52) seem to derive from secondary oxidation processes, which were able to mask the chemical composition attained at depth. On the other hand, the temperature estimates for Planchón–Peteroa and Descabezado Grande–Cerro Azúl fumaroles were consistent, although this similarity is only apparent since the $CO_2$–$CH_4$–$H_2$ equilibrium occurred at more oxidizing conditions ($R_H$ from $-3.2$ to $-3.0$) with respect to that controlled by the GT redox buffer. This would imply that these hydrothermal systems were characterized by thermally stratified fluid reservoirs, likely related to hot and oxidizing magmatic fluids they receive from below. Such input of magmatic fluids is consistent with the $\delta^{13}C$-$CO_2$, Rc/Ra and $CO_2$/$^3He$ values of the fumarolic gases. A magmatic fluid contribution should also have affected the water isotopic signature of the fumarolic condensates, which on the contrary seems not consistent with the "Andesitic water" field (Taran et al., 1989), possibly due to the masking effect due to vapor condensation that affects these fluid discharges (Fig. 6). To investigate this process, the isotopic composition of the
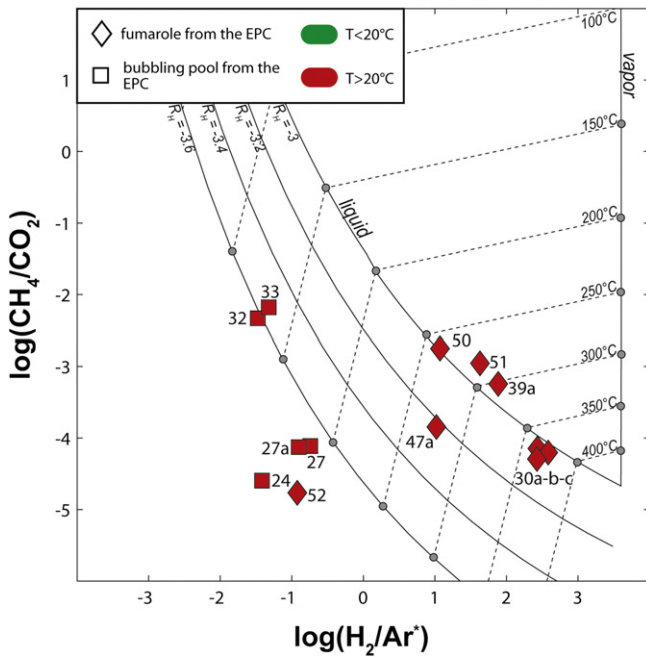
**Fig. 14.** Log($H_2$/*Ar) vs. log($CO_2$/$CH_4$) binary diagram for bubbling and fumarolic gases from Central Chile. Solid lines refer to equilibria in the vapor and liquid phases at temperatures from 150 to 350 °C and $R_H$ values from −3.0 to −3.6.

fumarolic vapor prior to condensation can be computed by considering two processes, as follows: i) $\delta^{18}O$-$H_2O$ fractionation due to $^{18}O$–$^{16}O$ exchange between water vapor and $CO_2$ and ii) the chemical and isotopic effect of vapor condensation (Benavente et al., 2013). As described by Chiodini et al. (2000), the former can be estimated, as follows:

$$\delta^{18}O - H_2O_{ini} = \delta^{18}O - H_2O + [2X_{CO2}/(1 + X_{CO2})] \\ \times [1000ln\alpha\,(T_i) - 1000ln\alpha\,(T_{meas})] \qquad (16)$$

where $T_i$ is temperature (°C) estimated by gas geothermometry in the $CO_2$–$CH_4$–$H_2$ systems (Fig. 14), $\delta^{18}O$-$H_2O_{ini}$ is the initial composition of steam at the $CO_2$–$CH_4$–$H_2$ equilibrium conditions, $T_{meas}$ is the fumarolic outlet temperature (°C), $X_{CO2}$ is the $CO_2$ molar fraction, and $\alpha$ is the oxygen isotope fractionation factor between $CO_2(g)$ and $H_2O(g)$, whose temperature (°C) dependence is given by:

$$1000ln\alpha = -5.7232 + 20.303(103/T) - 11.977\left(106/T^2\right) \\ + 3.7432\left(109/T^3\right). \qquad (17)$$

The $X_{CO2}$ values in Eq. (16) were calculated considering that $X_{CO2} + X_{H2O} \sim 1$ (Giggenbach, 1980) and using the $CO_2$/$H_2O$ molar ratios modeled from Eq. (6), where $r_{be}$ and $r_{af}$ correspond to the $CO_2$/$H_2O$ molar ratio before and after vapor condensation, and $\alpha$ is the $CO_2$–$H_2O$ liquid–vapor distribution factor (4651 at 100 °C; Giggenbach, 1980). As shown in Fig. 6, the corrected isotopic values (white diamonds) plot along a mixing line between meteoric water (at 4000 m a.s.l.) and the Andesitic water field, consistently with the vapor isotopic signature of the fluids discharged from the summit fumaroles of Tupungatito and Planchón–Peteroa volcanoes (Saltori et al., 2012; Benavente et al., 2013). The only exception was represented by sample 39a that was likely affected by condensation with a condensed steam fraction value (c = 1 − F) of 0.43.

## 6. Conclusions

The hydrothermal systems of the numerous fluid discharges seeping out along the Principal Cordillera of Central Chile are mainly fed by meteoric water infiltrating at different altitudes, the latter being dependent on the variable morphology of this large region. Significant contributions of magmatic water likely affected the hydrothermal fluids discharged from fumaroles fed by hydrothermal systems related to the active volcanoes. Thermal and cold springs in WPC were produced by interaction of groundwater, circulating through permeable pathways associated with the Infiernillo and San Ramon–Pocuro fault systems, and low soluble Cenozoic basaltic–andesitic volcanic rocks. This process exhaustively explains the low TDS, neutral to alkaline pH, shown by the springs having a $HCO_3^-$ dominated composition. The few $SO_4^{2-}$ and $Cl^-$ dominated waters of this area were produced by interaction, at relatively low temperatures (<60 °C), with the evaporite-rich Mesozoic formation possibly located underneath the Cenozoic rocks. Secondary mineral produced by the alteration of volcanic rocks, whose products are frequently recognized in this area, may also explain the relatively high $Cl^-$ concentrations in some thermal springs, although close to the boundary between WPC and EPC some addition of $Na^+$–$Cl^-$ brine cannot be excluded.

In EPC, the chemistry of thermal fluids was controlled by interaction with the Mesozoic sequences enhanced by addition of $CO_2$-rich gases, whose influence increases eastward approaching the active volcanic chain. At relatively short distance from the volcanoes showing fumarolic activity, direct interaction of shallow aquifers with $CO_2$($H_2S$)-rich volcanic gases produced immature $HCO_3^-$ and $SO_4^{2-}$ dominated waters. Closely out of these areas, especially S of the Maipo Orocline, where the dominating transtensional regime favors the uprising of heat and deep fluids, the occurrence of mature hydrothermal reservoirs at temperatures >200 °C was testified by the numerous thermal springs discharging high-TDS, $Na^+$–$Cl^-$ waters.

The He isotopic composition of fumarole and bubbling gases from the volcanic areas of Tinguiririca, Planchón–Peteroa and San José, as well as in the Mariposa geothermal area clearly indicated the occurrence of magmatic fluids. This was also suggested by the anomalous heat flux of these zones. However, the Rc/Ra values measured in these gases (up to 3.9), which were significantly lower than those measured from other hydrothermal systems in CVZ and SVZ (up to 6.9) and lower than the expected mantle signature for volcanic arcs (8 ± 1 Ra; Hilton et al., 2002), unequivocally indicated a significant addition of $^4He$-rich fluids from a crustal source. This process was reasonably occurring within the Andean crust during long-time residence (aging) of magma and/or contact with $^4He$-rich rocks. The $\delta^{13}C$-$CO_2$ (from −13.2 to −5.72‰ vs. V-PDB) and the $CO_2$/$^3He$ values (up to $14.6 \times 10^{10}$) also suggest that most $CO_2$ derived from limestone with an important contribution of sedimentary (organic-derived) carbon, both possibly originating from the recycling of subducted sediments and the sedimentary basement. In agreement with the information gathered from the preliminary prospection carried out at Calerías, Tinguiririca, Calabozos and Mariposa geothermal areas, the results of this study have confirmed the promising geothermal potential of this region that likely represents a complementary energy source able to provide an adequate response to the increasing need for energy supply of this country.

## References

Agusto, M., Tassi, F., Caselli, A., Vaselli, O., Rouwet, D., Capaccioni, B., Caliro, S., Chiodini, G., Darrah, T., 2013. Gas geochemistry of the magmatic-hydrothermal fluid reservoir in the Copahue–Caviahue Volcanic Complex (Argentina). J. Volcanol. Geotherm. Res. 257, 44–56.

Arriagada, C., Ferrando, R., Cordova, L., Morata, D., Roperch, P., 2013. The Maipo Orocline: a first scale structural feature in the Miocene to Recent geodynamic evolution in the central Chilean Andes. AndGeo 40 (3), 419–437.

Barazangi, M., Isacks, B.L., 1976. Spatial distribution of earthquakes and subduction of the Nazca plate beneath South America. Geology 4 (11), 686–692. http://dx.doi.org/10.1130/0091-7613(1976)4<686:SDOEAS>2.0.CO;2.

Barnett, P., 2012. Geothermal projects in South America of hot rock limited. 1st Chilean International Renewable Energy Congress, Santiago, Chile.

Benavente, O., Tassi, F., Gutiérrez, F., Vaselli, O., Aguilera, F., Reich, M., 2013. Origin of fumarolic fluids from Tupungatito Volcano (Central Chile): interplay between magmatic, hydrothermal, and shallow meteoric sources. Bull. Volcanol. 75 (8), 1–15. http://dx.doi.org/10.1007/s00445-013-0746-x.

Bencini, A., 1985. Applicabilità del metodo dell'Azometina-H alla determinazione del Boro nelle acque naturali. Rend. Soc. Ital. Mineral. Petrol. 40, 311–316.

Brondi, M., Dall'Aglio, M., Vitrani, F., 1973. Lithium as pathfinder element in the large scale hydrothermal exploration for hydrothermal systems. Geothermics 2, 142–153. http://dx.doi.org/10.1016/0375-6505(73)90021-7.

Caliro, S., Chiodini, G., Izzo, G., Minopoli, C., Signorini, A., Avino, R., Granieri, D., 2008. Geochemical and biochemical evidence of lake overturn and fish kill at Lake Averno, Italy. Journal of Volcanology and Geothermal Research. V. 178. I. 2, 305–316.

Cembrano, J., Lara, L., 2009. The link between volcanism and tectonics in the southern volcanic zone of the Chilean Andes: a review. Tectonophysics 471 (1–2), 96–113. http://dx.doi.org/10.1016/j.tecto.2009.02.038.

Charrier, R., Baeza, O., Elgueta, S., Flynn, J.J., Gans, P., Kay, S.M., Muñoz, N., Wyss, A.R., Zurita, E., 2002. Evidence for Cenozoic extensional basin development and tectonic inversion south of the flat-slab segment, southern Central Andes, Chile (33°–36°S.L.). J. S. Am. Earth Sci. 15 (1), 117–139. http://dx.doi.org/10.1016/S0895-9811(02)00009-3.

Chiodini, G., Marini, L., 1998. Hydrothermal gas equilibria: the $H_2O$–$H_2$–$CO_2$–CO–$CH_4$ system. Geochim. Cosmochim. Acta 62, 2673–2687. http://dx.doi.org/10.1016/S0016-7037(98)00181-1.

Chiodini, G., Frondini, F., Marini, L., 1995. Theoretical geothermometers and $pCO_2$ indicators for aqueous solutions coming from hydrothermal systems of medium-low temperature hosted in carbonate–evaporite rocks. Application to the thermal springs of the Etruscan Swell, Italy. Appl. Geochem. 10, 337–346. http://dx.doi.org/10.1016/0883-2927(95)00006-6.

Chiodini, G., Allard, P., Caliro, S., Parello, F., 2000. $^{18}O$ exchange between steam and carbon dioxide in volcanic and hydrothermal gases: isotopic and genetic implications. Geochim. Cosmochim. Acta 64, 2479–2488. http://dx.doi.org/10.1016/S0016-7037(99)00445-7.

Clavero, J., Pineda, G., Mayorga, C., Giavelli, A., Aguirre, I., Simmons, S., Martini, S., Soffia, J., Arriaza, R., Polando, E., Achurra, L., 2011. Geological, geochemical, geophysical and first drilling data from Tinguiririca geothermal area, central Chile. Geothermal Resources Council Transactions (GRC) 35. Geothermal Resources Council, San Diego, California, pp. 731–734.

Cox, S.F., 2010. The application of failure mode diagrams for exploring the roles of fluid pressure and stress states in controlling styles of fracture-controlled permeability enhancement in faults and shear zones. Geofluids 10 (1–2), 217–233. http://dx.doi.org/10.1111/j.1468-8123.2010.00281.x.

Davis, S.N., Cecil, L.D., Zreda, M., Moysey, S., 2001. Chlorine-36, bromide, and the origin of spring water. Chem. Geol. 179, 3–16. http://dx.doi.org/10.1016/S0009-2541(01)00312-6.

Delany, J.M., Lundeen, S.R., 1991. The LLNL thermochemical data base — revised data and file format for the EQ3/6 package (Other Information: PBD: Jul 1991: Medium: P; Size: 59 pp.).

Dobson, P., Kennedy, M., Reich, M., Sanchez, P., 2013. Effects of Volcanism, Crustal Thickness, and Large Scale Faulting on the He Isotope Signatures of Geothermal Systems in Chile. Thirty-Eighth Workshop on Geothermal Reservoir Engineering Stanford University, Stanford, California February 11-13, SGP-TR-198.

Droguett, B., Morata, D., Clavero, J., Pineda, G., Morales, S., Carrillo, F., 2012. Mineralogía de alteración en el pozo Pte-1, campo geotermal Tinguiririca, Chile. XIII Congreso Geológico Chileno 13. Universidad Católica del Norte, E. Medina. Antofagasta, Chile, pp. 500–502 (In Spanish).

Dufey, A., 2010. Opportunities and domestic barriers to clean energy investment in Chile. IISD: Trade, Investment and Climate Change Series (Available in http://www.iisd.org/pdf/2010/bali_2_copenhagen_Chile_Jun2010.pdf).

Epstein, S., Mayeda, T.K., 1953. Variation of the $^{18}O/^{16}O$ ratio in natural waters. Geochim. Cosmochim. Acta 4, 213–224. http://dx.doi.org/10.1016/0016-7037(53)90051-9.

Evans, W.C., White, L.D., Rapp, J.B., 1988. Geochemistry of some gases in hydrothermal fluids from the southern Juan de Fuca Ridge. J. Geophys. Res. Solid Earth 93 (B12), 15305–15313. http://dx.doi.org/10.1029/JB093iB12p15305.

Farías, M., Charrier, R., Carretier, S., Martinod, J., Fock, A., Campbell, D., Cáceres, J., Comte, D., 2007. Late Miocene high and rapid surface uplift and its erosional response in the Andes of Central Chile (33°–35°S). Tectonics 27 (1), TC1005. http://dx.doi.org/10.1029/2006TC002046.

Farías, M., Comte, D., Charrier, R., Martinod, J., David, C., Tassara, A., Tapia, F., Fock, A., 2010. Crustal-scale structural architecture in central Chile based on seismicity and surface geology: implications for Andean mountain building. Tectonics 29, 22. http://dx.doi.org/10.1029/2009TC002480.

Fontes, J.C., Matray, J.M., 1993. Geochemistry and origin of formation brines from the Paris Basin, France. Chem. Geol. 109, 177–200. http://dx.doi.org/10.1016/0009-2541(93)90068-T.

Fournier, R.O., 1979. A revised equation for the Na/K geothermometer. Trans. Geotherm. Resour. Counc. 3, 221–224.

Fournier, R.O., Potter II, R.W., 1978. A magnesium correction for the Na–K–Ca geothermometer. Geochim. Cosmochim. Acta 43, 1543–1550. http://dx.doi.org/10.1016/0016-7037(79)90147-9.

Fournier, R.O., Truesdell, A.H., 1973. An empirical Na–K–Ca geothermometer for natural waters. Geochim. Cosmochim. Acta 37, 1255–1275. http://dx.doi.org/10.1016/0016-7037(73)90060-4.

Giambiagi, L.B., Ramos, V.A., Godoy, E., Alvarez, P.P., Orts, S., 2003. Cenozoic deformation and tectonic style of the Andes, between 33° and 34° south latitude. Tectonics 22 (4), 1041. http://dx.doi.org/10.1029/2001TC001354.

Giambiagi, L., Tassara, A., et al., 2014. Evolution of shallow and deep structures along the Maipo–Tunuyan transect (33°40′S): from the Pacific coast to the Andean foreland. In: Sepúlveda, S.A., Giambiagi, L.B., Moreiras, S.M., Pinto, L., Tunik, M., Hoke, G.D., Farías, M. (Eds.), Geodynamic Processes in the Andes of Central Chile and Argentina. Geological Society, London, Special Publications 399. http://dx.doi.org/10.1144/SP399.14.

Giggenbach, W.F., 1975. A simple method for the collection and analysis of volcanic gas samples. Bull. Volcanol. 39 (1), 132–145. http://dx.doi.org/10.1007/BF02596953.

Giggenbach, W.F., 1980. Geothermal gas equilibria. Geochim. Cosmochim. Acta 44, 2021–2032. http://dx.doi.org/10.1016/0016-7037(80)90200-8.

Giggenbach, W.F., 1987. Redox processes governing the chemistry of fumarolic gas discharges from White Island, New Zealand. Appl. Geochem. 2, 143–161. http://dx.doi.org/10.1016/0883-2927(87)90030-8.

Giggenbach, W.F., 1988. Geothermal solute equilibria. Derivation of Na–K–Mg–Ca geoindicators. Geochim. Cosmochim. Acta 52 (12), 2749–2765. http://dx.doi.org/10.1016/0016-7037(88)90143-3.

Giggenbach, W.F., 1991. Chemical techniques in geothermal exploration. In: D'Amore, F. (Ed.), Application of Geochemistry in Geothermal Reservoir Development. UNITAR, pp. 119–144.

Giggenbach, W.F., 1992. The composition of gases in geothermal and volcanic systems as a function of tectonic setting. Proc Int Symp Water–Rock Interaction 8, pp. 873–878.

Giggenbach, W.E., Goguel, R.L., 1989. Collection and analysis of geothermal and volcanic water and gas samples. NZ DSIR Report No CD 2401 (Appendix), p. 81.

Gripp, A.E., Gordon, R.G., 2002. Young tracks of hotspots and current plate velocities. Geophys. J. Int. 150 (2), 321–361. http://dx.doi.org/10.1046/j.1365-246X.2002.01627.x.

Hall, S., Román, R., Cuevas, F., Sanchez, P., 2009. Are dams necessary in Patagonia? An Analysis of Chile's Energy Future. Ocholibros Ed (in Spanish)

Hamza, V.M., Muñoz, M., 1996. Heat flow map of South America. Geothermics 25 (6), 599–621. http://dx.doi.org/10.1016/S0375-6505(96)00025-9.

Hardie, L.A., 1983. Origin of $CaCl_2$ brines by basalt–seawater interaction: insights provided by some simple mass balance calculations. Contrib. Mineral. Petrol. 82, 205–213. http://dx.doi.org/10.1007/BF01166615.

Hauser, A., 1997. Catastro y caracterización de las fuentes de aguas minerales y termales de Chile Santiago, Chile, Servicio Nacional de Geología y Minería (SERNAGEOMIN). Boletín 50 70 pp. (In Spanish).

Hickson, C.J., Ferraris, F., Rodriguez, C., Sielfeld, G., Henriquez, R., Gislason, T., Selters, J., Benoit, D., White, P., Southon, J., Ussher, G., Smith, A., Lovelock, B., Lawless, J., Quinliven, P., Smith, L, Yehia, R., 2011. The Mariposa geothermal system, Chile. Geothermal Resources Council Transactions (GRC) 35. Geothermal Resources Council, San Diego, California, pp. 817–825.

Hildreth, W., Moorbath, S., 1988. Crustal contributions to arc magmatism in the Andes of Central Chile. Contrib. Mineral. Petrol. 98 (4), 455–489. http://dx.doi.org/10.1007/BF00372365.

Hilton, D.R., 1996. The helium and carbon isotope systematics of a continental geothermal system: results from monitoring studies at Long Valley caldera (California, U.S.A.). Chem. Geol. 127, 269–295. http://dx.doi.org/10.1016/0009-2541(95)00134-4.

Hilton, D.R., Hammerschmidt, K., Teufel, S., Friedrichsen, H., 1993. Helium isotope characteristics of Andean geothermal fluids and lavas. Earth Planet. Sci. Lett. 120 (3–4), 265–282. http://dx.doi.org/10.1016/0012-821X(93)90244-4.

Hilton, D.R., Fischer, T.P., Marty, B., 2002. Noble gases and volatile recycling at subduction zones. In: Porcelli, D., Ballentine, C.J., Wieler, R. (Eds.), Noble Gases in Cosmochemistry and Geochemistry. Mineralogical Society of America, Washington, pp. 319–370 http://dx.doi.org/10.2138/rmg.2002.47.9.

Hodgson, S., 2013. Focus on Chile parts I, II and III 47. Geothermal Resources Council Bulletin (GRC).

Hoefs, J., 1997. Stable Isotope Geochemistry. 4th ed. Springer, Verlag, Berlin, Germany, p. 201.

Hoke, G.D., Aranibar, J.N., Viale, M., Araneo, D.C., Llano, C., 2013. Seasonal moisture sources and the isotopic composition of precipitation, rivers, and carbonates across the Andes at 32.5–35.5°S. Geochem. Geophys. Geosyst. 14 (4), 962–978. http://dx.doi.org/10.1002/ggge.20045.

Horita, J., Wesolowski, D.J., 1994. Liquid-vapor fractionation of oxygen and hydrogen isotopes of water from the freezing to the critical temperature. Geochim. Cosmochim. Acta 58, 3425–3437.

Langelier, W.F., Ludwig, H.F., 1942. Graphical methods for indicating the mineral character of natural waters. JAWWA 34, 335.

Maksaev, V., Townley, B., Palacios, C., Camus, F., 2007. Metallic ore deposits. In: Moreno, T., Gibbons, W. (Eds.), The Geology of Chile. The Geological Society (London), p. 414.

Mamyrin, B., Tolstikhin, I., 1984. Helium isotopes in nature. Developments in Geochemistry. E. S. Ltd. Amsterdam, Elsevier, p. 288.

Mariner, R.H., Evans, W.C., Presser, T.S., White, L.D., 2003. Excess nitrogen in selected thermal and mineral springs of the Cascade Range in northern California, Oregon and Washington: sedimentary or volcanic in origin? J. Volcanol. Geotherm. Res. 121, 99–114. http://dx.doi.org/10.1016/S0377-0273(02)00414-6.

Marini, L., 2006. Chapter 5: The product solid phases. Geological sequestration of carbon dioxide: thermodynamics, kinetics, and reaction path modeling. D. i. Geochemistry 11. Elsevier, pp. 79–167. http://dx.doi.org/10.1016/S0921-3198(06)80025-6.

Marini, L., Chiodini, G., Cioni, R., 1986. New geothermometers for carbonate–evaporite geothermal reservoirs. Geothermics 15, 77–86. http://dx.doi.org/10.1016/0375-6505(86)90030-1.

Marini, L., Ottonello, G., Canepa, M., Cipolli, F., 2000. Water–rock interaction in the Bisagno valley (Genoa, Italy): application of an inverse approach to model spring water chemistry. Geochim. Cosmochim. Acta 64 (15), 2617–2635. http://dx.doi.org/10.1016/S0016-7037(00)00383-5.

Montegrossi, G., Tassi, F., Vaselli, O., Buccianti, A., Garofalo, K., 2001. Sulfur species in volcanic gases. Anal. Chem. 73 (15), 3709–3715. http://dx.doi.org/10.1021/ac001429b.

Mook, W.G., Bommerson, J.C., Staverman, W.H., 1974. Carbon isotope fractionation between dissolved bicarbonate and gaseous carbon dioxide. Earth Planet. Sci. Lett. 22, 169–176.

Muñoz, M., Aguirre, L., Vergara, M., Demant, A., Fuentes, F., Fock, A., 2010. Prehnite–pumpellyite facies metamorphism in the Cenozoic Abanico Formation, Andes of central Chile (33°50′S): chemical and scale controls on mineral assemblages, reaction progress and the equilibrium state. AndGeo 37 (1), 54–77.

Ohmoto, H., Goldhaber, M.B., 1997. Sulfur and carbon isotopes. In: Barnes, H.L. (Ed.), Geochemistry of Hydrothermal Ore Deposits. John Wiley & Sons, pp. 517–611.

Ozima, M., Podosek, F.A., 1983. Noble gas geochemistry. Cambridge University Press, Cambridge.

Pauwels, H., Fouillac, C., Goff, F., Vuataz, F.D., 1997. The isotopic and chemical composition of CO$_2$-rich thermal waters in the Mont–Dore region (Massif-Central, France). Appl. Geochem. 12 (4), 411–427. http://dx.doi.org/10.1016/S0883-2927(97)00010-3.

Peiffer, L., Bernard-Romero, R., Mazot, A., Taran, Y.A., Guevara, M., Santoyo, E., 2014. Fluid geochemistry and soil gas fluxes (CO$_2$–CH$_4$–H$_2$S) at a promissory hot dry rock geothermal system: the Acoculco caldera, Mexico. J. Volcanol. Geotherm. Res. 284 (122–137), 2014. http://dx.doi.org/10.1016/j.jvolgeores.2014.07.019.

Pilger, R.H., 1981. Plate reconstruction, aseismic ridges, and low angle subduction beneath the Andes. Geol. Soc. Am. Bull. 92, 448–456. http://dx.doi.org/10.1130/0016-7606(1981)92<448:PRARAL>2.0.CO;2.

Poreda, R., Craig, H., 1989. Helium isotope ratios in circum-Pacific volcanic arcs. Nature (London) 338, 473–478. http://dx.doi.org/10.1038/338473a0.

Ray, M., Hilton, D., Muñoz, J., Fischer, T., Shaw, A., 2009. The effects of volatile recycling, degassing and crustal contamination on the helium and carbon geochemistry of hydrothermal fluids from the southern volcanic zone of Chile. Chem. Geol. 266 (1–2), 38–49. http://dx.doi.org/10.1016/j.chemgeo.2008.12.026.

Reyes, A.G., Christenson, B.W., Faure, K., 2010. Sources of solutes and heat in low-enthalpy mineral waters and their relation to tectonic setting, New Zealand. J. Volcanol. Geotherm. Res. 192, 117–141. http://dx.doi.org/10.1016/j.jvolgeores.2010.02.015.

Rizzo, A., Barberi, F., Carapezza, M.L., Di Piazza, A., Francalanci, L., Sortino, F., D'Alessandro, W., 2015. New mafic magma refilling a quiescent volcano: evidence from He–Ne–Ar isotopes during the 2011–2012 unrest at Santorini, Greece. Geochem. Geophys. Geosyst. http://dx.doi.org/10.1002/2014GC005653.

Rollinson, H., 1993. Using geochemical data. Longman, London, UK, p. 352.

Saltori, O., Aguilera, F., Agusto, M., Benavente, O., Tassi, F., Caselli, A., Gutierrez, F., Pizarro, M., 2012. Fluids geochemistry from Planchón–Peteroa–Zufre volcanic complex, southern volcanic zone, Chile. XIII Congreso Geológico Chileno. E. Medina 13. Universidad Católica del Norte, Antofagasta, Chile, pp. 474–476.

Sanchez-Alfaro, P., Sielfeld, G., Van Campen, B., Dobson, P., Fuentes, V., Reed, A., Palma-Behnke, R., Morata, D., 2015. Geothermal barriers, policies and economics in Chile — lessons for the Andes. Renew. Sust. Energ. Rev. 51, 1390–1401. http://dx.doi.org/10.1016/j.rser.2015.07.001.

Sano, Y., Williams, S.N., 1996. Fluxes of mantle and subducted carbon along convergent plate boundaries. Geophysical Research Letters (ISSN: 0094-8276) 23. http://dx.doi.org/10.1029/96GL02260.

Sano, Y., Fischer, T.P., 2013. The analysis and interpretation of noble gases in modern hydrothermal systems. In: Burnard, P. (Ed.), The Noble Gases as Geochemical Tracers. Springer Verlag, Berlin Heidelberg, pp. 249–317 http://dx.doi.org/10.1007/978-3-642-28836-4_10.

Sano, Y., Marty, B., 1995. Origin of carbon in fumarolic gases from island arcs. Chem. Geol. 119, 265–274. http://dx.doi.org/10.1016/0009-2541(94)00097-R.

Sibson, R.H., 1996. Structural permeability of fluid-driven fault-fracture meshes. J. Struct. Geol. 18 (8), 1031–1042. http://dx.doi.org/10.1016/0191-8141(96)00032-6.

Sibson, R.H., 2007. An episode of fault-valve behaviour during compressional inversion?: the 2004 MJ6.8 Mid-Niigata Prefecture, Japan, earthquake sequence. Earth Planet. Sci. Lett. 257 (1–2), 188–199. http://dx.doi.org/10.1016/j.epsl.2007.02.031.

Snyder, G., Poreda, R., Fehn, U., Hunt, A., 2003. Sources of nitrogen and methane in central American geothermal settings: noble gas and $^{129}$I evidence for crustal and magmatic volatile components. Geochem. Geophys. Geosyst. http://dx.doi.org/10.1029/2002GC000363.

Soffia, J., 2004. Perspectivas de Desarrollo de la Energía Geotérmica en Chile. En: Seminario Latinoamericano sobre energías renovables: Hacia la Conferencia Mundial de Bonn — 2004. Programa Chile Sustentable, pp. 93–100 (M. [en línea] http://www.archivochile.com/Chile_actual/patag_sin_repre/06/chact_hidroay-6%2000011.pdf, in spanish).

Stern, C.M.H., López-Escobar, L., Clavero, J., Lara, L., Naranjo, J., Parada, M., Skewes, A., 2007. Chilean volcanoes. Geological Society Special Publication: The Andes of Chile. Londres, pp. 147–178.

Stevenson, S., 1993. Physical models of fumarolic flow. J Volcanol Geotherm 57 (3–4), 139–156.

Taran, Y.A., 2005. A method for determination of the gas–water ratio in bubbling springs. Geophys. Res. Lett. 32, L23403. http://dx.doi.org/10.1029/2005GL024547.

Taran, Y.A., Pokrovsky, B.G., Esikov, A.D., 1989. Deuterium and oxygen-18 in fumarolic steam and amphiboles from some Kamchatka volcanoes: "andesitic waters". Dokl. Akad. Nauk SSSR 304, 440–443.

Tassara, A., Gotze, H.J., Schmidt, S., Hackney, R., 2006. Three-dimensional density model of the Nazca plate and the Andean continental margin. J. Geophys. Res. Solid Earth 111 (B9). http://dx.doi.org/10.1029/2005JB003976.

Truesdell, A.H., Hulston, J.R., JCh, F., 1980. Isotopic evidence on environments of geothermal systems. In: Fritz, P. (Ed.), Handbook of Environmental Isotopes Geochemistry.The Terrestrial Environment A 1. Elsevier, Amsterdam, pp. 179–226

Vaselli, O., Tassi, F., Montegrossi, G., Capaccioni, B., Giannini, L., 2006. Sampling and analysis of fumarolic gases. Acta Vulcanol. 18, 65–76.

Vergara, M., Levi, B., Villarroel, R., 1993. Geothermal-type alteration in a burial metamorphosed volcanic pile, central Chile. J. Metamorph. Geol. 11, 449–454. http://dx.doi.org/10.1111/j.1525-1314.1993.tb00161.x.

Yáñez, G., Ranero, C.R., von Huene, R., Díaz, J., 2001. Magnetic anomaly interpretation across the southern central Andes (32°–34°S): the role of the Juan Fernández Ridge in the late Tertiary evolution of the margin. J. Geophys. Res. 106, 6325–6345. http://dx.doi.org/10.1029/2000JB900337.